Chapter 3

Physico-Chemical Characteristics of Gold Nanoparticles

Vincenzo Amendola[1], Moreno Meneghetti[1], Mauro Stener[5], Yan Guo[2,3], Shaowei Chen[3], Patricia Crespo[4], Miguel Angel García[4], Antonio Hernando[4], Paolo Pengo[5] and Lucia Pasquato[5,*]

[1] *Department of Chemical Sciences, University of Padova, Padova, Italy;* [2] *School of Environmental Science and Engineering, Nanjing University of Information Science and Technology, Nanjing, Jiangsu, P. R. China;* [3] *Department of Chemistry and Biochemistry, University of California, Santa Cruz, CA, USA;* [4] *Instituto de Magnetismo Aplicado and Dpto. Física de Materiales, Universidad Complutense de Madrid, Madrid, Spain;* [5] *Department of Chemical and Pharmaceutical Sciences, University of Trieste, Trieste, Italy*

**Corresponding author: E-mail: lpasquato@units.it*

Chapter Outline

Gold Nanoparticles in Analytical Chemistry. http://dx.doi.org/10.1016/B978-0-444-63285-2.00003-1

1. INTRODUCTION

Considering their size and surface functionalization, gold nanoparticles may be divided into three main groups: gold colloids, gold nanoparticles protected by an organic monolayer (MPCs), and small gold clusters.

Gold colloids are large metal particles with a size range of 10–100 nm, usually obtained by reduction of Au(III) salts in the presence of mild reducing agents, most commonly, trisodium citrate in procedures created by Turkevich

and Frens and improved by Natan [1]. The resulting particles are stabilized against aggregation by electrostatic repulsion as a result of the surface-adsorbed citrate. This stabilization, being electrostatic in nature, does not allow the use of colloids in media of elevated ionic strength; the additions of salts to a colloidal solution results in irreversible aggregation. However, gold colloids may be stabilized by adsorption of a wide variety of compounds such as proteins or polymers but also by interaction with other compounds such as thiols that form a compact, self-assembled monolayer on their surface. In describing the structure of colloids, it must be stressed that the syntheses of these compounds is very often carried out under kinetic rather than thermodynamic control. These conditions do not allow obtaining the most stable structure possible in the reaction conditions employed. As a consequence, the preparations of gold colloids frequently contain particles with a large variety of shapes and typically are polydispersed with a relatively large distribution of sizes. However, procedures for the obtainment of gold nanorods, nanocubes, nanoboxes, nanobranches, and nanobipyramids are available; generally, these procedures rely on the use of specific surface modifiers and seeds during the synthesis.

Monolayer protected clusters (MPCs) are particles with a gold core with a size in the range of 1−10 nm surrounded by a monolayer of strongly chemisorbed ligands; the most studied systems are stabilized by thiols. The resulting materials are very stable, owing to the strength of the gold−sulfur bond that is about 208 kJ/mol. MPCs became available after the synthesis developed by Brust and Schiffrin in 1994. At variance with colloids, MPCs are stable in solution and in the solid state. The presence of the passivating monolayer prevents irreversible aggregation and imparts solubility in a broad range of solvents including aqueous solutions and biological media. MPCs are, in general, prepared under kinetic control, polydispersity is typical, and metal cores with different shapes with a varying extent of twinning are common. Only recently, a theoretical thermodynamic analysis aimed at identifying the most stable morphologies of small gold nanoparticles was performed, indicating that the equilibrium shapes not only depend on the temperature but also on the size of the particles, with well-defined shape transitions occurring at certain critical sizes. In general, the most stable shapes of the particles are those with the preferential development of low energy facets. Small gold clusters represent the "lower bound" of MPCs; these are molecular entities comprising a few tens of atoms and are typically "atomically precise" or strictly monodispersed. The monodispersity of these species is the result of their inherent stability; in several cases, the preparation of small gold clusters relies on a "size focusing" or "thiol etching" process that converts polydispersed mixtures of unstable clusters to the most stable ones. The monodispersity of these systems enables their crystallization and the obtainment of several X-ray structures of gold-thiolate clusters that are so far unreported for larger MPCs.

1.1 Physical Properties, Chemical Properties, and Their Size Dependence

The physical properties of gold nanoparticles are strongly influenced by their size because the electronic structure of the gold particles changes with size and shape. Small gold clusters feature large band gaps, while in larger particles the valence electrons may be described in the framework of the *jellium* model. A clear example of this transition can be obtained by inspection of the electronic absorption spectra of these materials. The dominating optical feature of AuNPs with size of 2−100 nm is the surface plasmon resonance (SPR) which confers the characteristic bright red color to colloidal solutions of spherical AuNPs. This has attracted the interest of manufacturers since ancient times for the realization of ornamental cups, glass, and luster plates. Compared to other organic and inorganic chromophores, AuNPs with a size above about 2 nm have larger extinction cross-sections, with a possibility of reaching 100% of light-to-heat conversion efficiency, high photostability, and the ability to amplify the electromagnetic field near the metal surface. On the contrary, for smaller clusters, well-defined and specific absorption features are observed. Small thiolate-protected gold nanoparticles exhibit ferromagnetic-like behavior that is in stark contrast to the diamagnetism of bulk gold and of weakly protected nanoparticles. Another effect associated with the reduction of the nanoparticle size is the onset of quantized (single electron) charging with the nanoparticles behaving as nanoscale molecular capacitors. The chemical properties of gold nanoparticles and their catalytic activity are also strongly dependent on their size and shape. In addition, the nanoparticle size is one of the parameters governing the formation of domains with well-defined morphology on the monolayer of MPCs. In the following sections, an in-depth discussion on the properties of gold nanoparticles will be presented.

In this chapter, we discuss the relevant physical and chemical properties of gold nanoparticles that are exploited for analytical applications in a variety of different fields. This chapter was conceived to collect in a single place an overview of the properties of gold nanoparticles that are important for technological applications, with prevalent reference to the scientific literature that has appeared in the last six years. Given the extremely broad expertise needed for an in-depth discussion, the chapter is co-authored with experts in the specific field dealing with optical properties, ab initio calculations of electronic properties, magnetic, electrochemical and chemical properties.

2. OPTICAL PROPERTIES

2.1 Origin of the Surface Plasmon Absorption

Collective oscillations of conduction electrons in metals are known as *plasmons* [2,3]. According to the Fermi liquid model, plasmons can be satisfactorily described as a negatively charged electron cloud displaced

from its equilibrium position around a lattice made of positively charged ions, in analogy to a real plasma [2,3]. Excitation of bulk plasmons by photons is not allowed since the energy dispersion curves of plasmons and photons never cross each other [2,3]. However, the presence of a surface in real materials allows the existence of new plasmon modes, called surface plasmons, which can be excited by electromagnetic waves [2,3]. In particular, localized surface plasmons are observed in metal nanoparticles, which are nonpropagating collective excitations of conduction electrons. Therefore, they differ from surface plasmon-polaritons, which are propagating plasmon modes allowed on the surface of bulk metals and periodic metallic patterns [2]. When AuNP size is small compared to the resonant electromagnetic wavelength, the electric field distribution along the particle is uniform, electron cloud polarization is coherent in each point of the metal, and dipolar plasmon oscillations are excited [3]. When AuNP size is comparable to the resonant electromagnetic wavelength, the electric field distribution along the particle is nonuniform, electron cloud polarization is no more coherent in each point of the metal, and multipolar plasmon oscillations are excited [3].

Surface plasmons in single-metal nanoparticles can be directly probed by electron energy loss spectroscopy (EELS), cathodoluminescence, and far field extinction microscopy, while the plasmon response of ensembles of AuNPs can be detected by optical absorption spectroscopy [2–5]. In the optical absorption spectrum of a dispersion of spherical AuNPs (Figure 1(A)), the SPR is centered around 520 nm, and it is partially overlapped with the absorption originated by interband transitions, namely by single electron optical

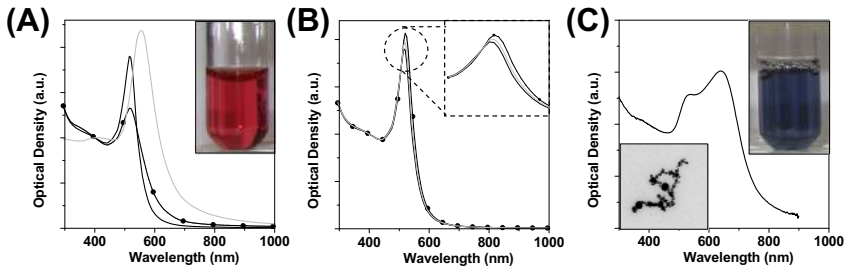

FIGURE 1 (A) Optical absorption spectra for AuNPs with size of 4 nm (black circles), 30 nm (black line), and 100 nm (grey line) in water. All spectra are scaled to 1:400 nm for clarity. Damping of SPR is observed in the 4 nm AuNPs due to intrinsic size effects, while red shift and broadening are observed in the 100 nm AuNPs due to extrinsic size effects. Inset shows the typical purple color of a AuNP colloid. (B) The SPR of a 30 nm AuNP solution in water (black line) is red shifted and slightly broadened when the medium refractive index is increased 2.5% (grey line) and 5% (black circles). Inset shows a magnification of the SPR. (C) The SPR is sensibly red shifted and broadened in aggregates of AuNPs, as those shown in the TEM image. To the naked eye, this effect is perceived as a shift to violet-blue (see inset).

excitations from the occupied 5d band to the unoccupied levels of the 6s−6p band of the metal [3,4]. The SPR intensity scales with the number of conduction electrons in the AuNP, where each gold atom contributes one conduction electron [4], and this accounts for their incredibly high extinction cross-section, which is 10^5 times larger than that of organic chromophores for a 20 nm AuNP [2,6].

The plasmon extinction band detected in the optical absorption spectra of AuNPs dispersions is originated by the sum of scattered and absorbed photons, with a proportion strongly dependent on particle size [2,3]. For AuNPs with size $d \ll \lambda$, where λ is the wavelength of the electromagnetic radiation, the absorption dominates over scattering [2,3]. However, scattering and absorption scale with the 6th and the 3rd power of a particle's size, respectively. Therefore, the two effects become comparable for 50 nm AuNPs, whereas scattering prevails above this size [2,3].

2.2 Specific Phenomena Influencing the Surface Plasmon Absorption

The SPR is primarily affected by particle size, shape, and physical−chemical environment, including the reciprocal distance between particles [2,3]. The size effects influencing the SPR are divided into extrinsic and intrinsic (Figure 1(A)) [3]. The extrinsic size effect is a retardation effect due to the excitation of multipolar plasmon modes when nanoparticle size increases toward the resonant electromagnetic wavelength [2,3]. The extrinsic size effect is a bare electromagnetic phenomenon appearing in the optical absorption spectrum as broadening and red shift of the SPR for increasing AuNP size [2,3]. The multipolar excitations are dominant for AuNPs larger than 60 nm, whereas dipolar oscillations dominate for particles of 25 nm or smaller [2,3].

Intrinsic size effects are due to the modification of the metal optical constant when AuNP size is below 30 nm [3]. The optical constant changes because of additional contributions to the free electron relaxation when the nanoparticle size is reduced [3]. In particular, the free electron scattering at particle surface is no more negligible when conduction electrons mean free path ($\sim$40 nm for Au) becomes comparable to particle size [2,3]. This scattering contribution overshadows other phenomena originated by changes in the phonons spectra, quantum size effects, changes in the phonon−electron coupling for the high surface charge during plasmon oscillation, and so on. In the optical absorption spectrum, the intrinsic size effect increases the decay rate of the SPR and, consequently, it damps for decreasing particle's size, with almost complete quenching of the plasmon band in AuNPs smaller than 2 nm [2,3].

The width, position, and number of SPRs are determined by the shape of the AuNPs [2,6]. Spherical particles have only one SPR, whereas cigar-like

structures have two plasmon modes, resonating at different wavelengths and corresponding to the collective excitation of conduction electrons along the two axes of the rod [5]. By further lowering the symmetry of the Au nanostructure, new plasmon modes may arise [2,6]. A common feature of these new SPRs is that they are red shifted compared to that of spheres [3]. For instance, the red shift of the SPR corresponding to longitudinal excitation of Au rods by the electromagnetic field increases with the aspect ratio of the rod [5].

The physical-chemical environment influences the SPR in several ways. Regarding the chemical effects, the most intense mechanism is called chemical interface damping (CID) [3]. CID produces a sensible widening and red shift of the SPR when adsorbates are present on a particle's surface [3].

This holds both for chemisorption, as in the case of thiol-stabilized nanoparticles, and for physisorption, as in the case of citrate- or alkylamine-stabilized nanoparticles [3]. The SPR broadening due to CID is explained considering that adsorbates offer new relaxation pathways for both excited electrons and phonons in the metal [3]. Persson developed a model in which the empty lowest unoccupied molecular orbitals (LUMOs) of adsorbates are coupled with conduction band electrons [3]. During plasmon oscillation, the reversible electron transfer into LUMOs is possible, originating fast loss of coherence with other excited electrons and a larger bandwidth [3]. Different adsorbates have different LUMO position, then couple in a different way with the metal conduction band and originate different SPR widths [3]. Regarding the physical effects, the position, width, and intensity of the SPR are sensitive to the dielectric properties of the environment [2,3]. In AuNPs dispersed in a homogeneous transparent matrix, for example, a liquid solution or a polymeric matrix, the increase in the refractive index of the medium will correspond to an increase in intensity, red shift, and full width at half maximum (FWHM) of the SPR (Figure 1(B)) [3]. In the case of AuNPs coated with ligands, the same effect on the SPR will be observed as a function of the polarizability of the surrounding layer [2].

Moreover, plasmons on distinct nanoparticles can reciprocally influence each other, depending on the particle's distance, geometry, and relative photon polarization [2,6]. In general, multimers of spheres have new SPR because, when the nanoparticle separation decreases, the plasmons of individual nanoparticles begin to interact and hybridize with the plasmons of the other particles [2,6]. In the case of dimers, plasmon hybridization produces an SPR red shift that decays near-exponentially with the interparticle gap over a distance that is roughly 0.2 times the particle size, independent of the nanoparticle size, shape, material, and the medium dielectric constant [7].This universal decaying behavior of the SPR in nanoparticle pairs originates from the distance decay of the interparticle near-field that couples the particles

together [7]. When nanoparticles are in conductive contact, the hybridization effects disappear and the SPR abruptly blue shifts to that of a particle with necklace shape [7,8].

2.3 Sensing by Surface Plasmon Absorption

The SPR finds large applications for chemical and biological sensing due to sensitive spectral response to the local surface environment, photostability, and ease of monitoring the light signal because of the large scattering and absorption cross-sections [9].The spectral sensitivity, defined as the relative shift in resonance wavelength with respect to the refractive index change of surrounding materials, is dependent on the SPR position and width, which in turn depends on metal type and on particle shape [9]. This determines a long spatial range of the decaying electromagnetic field, allowing appreciable sensitivity up to a distance of 40 nm [9]. In general, a linear relationship between the absorption or scattering band position and the surrounding refraction index exists, with a slope of about 100 nm for refraction index unit [9].

One of the most important features for a sensor is selectivity, which can be conferred to AuNPs by appropriate engineering of their surface, based on the reactivity of Au atoms with thiols and disulfides. Usually, AuNPs are functionalized with a specific molecular receptor for a target molecule capable of producing an appreciable red shift of the SPR after the change in the surrounding refraction index of metal nanoparticles upon binding of the target molecule [5]. This approach is similar to enzyme-linked immunosorbent assay (ELISA), the difference lying in that ELISA requires a second, specific fluorescent label that is able to bind the target in a sandwich structure. Whereas, these localized surface plasmon assays exploit only one binding event [8].

On the other hand, ELISA-like colorimetric sensors, based on AuNPs, have also been developed for the detection of analytes which can be coordinated on two ends [10]. In this case, the substrate and the AuNPs are both coated with a targeting molecule, for example, an antibody selective for the target protein, and the substrate is decorated with AuNPs in the presence of the analyte, with a consequent change in color from white to red-brownish [10].

Plasmon coupling in nearby AuNPs is also exploited in molecular rulers based on the SPR dependence on the distance between two metal nanoparticles [11]. Plasmon molecular rulers have been applied to the real-time sensing of DNA hybridization processes as well as to DNA folding in the presence of different saline buffers [10]. In particular, the SPR sensitivity on the coupling distance of two metal nanoparticles is so high that each step of dimer formation is measurable, included elastic recoil after the first contact [10]. AuNP of 40 nm in diameter allows monitoring distances up to 70 nm by far-field extinction microscopy of a single dimer [10].

The SPR changes due to plasmon hybridization in AuNPs aggregates can be also exploited for colorimetric assays [10]. In agglomerates of AuNPs made by tens of particles, plasmon hybridization originates two main bands, one close to the original sphere's position and another red-shifted, both sensibly broader than single-particle SPR (Figure 1(C)) [8,10,12]. When particles in the aggregates are several hundred, only one very broad red-shifted band is present [2,6,8,12]. In a typical strategy, metal nanoparticles in solution are coated with specific receptors, for instance, with single-stranded DNA polynucleotides or appositely designed peptides, which promote particle aggregation and sensible change in the color of the solution only in the presence of the target biomolecules [6,10]. This method allows analyte detection limits from femtomoles to nanomoles [6,10]. In the case of DNA detection, the target polynucleotide bridges two particles during the hybridization process with receptor oligonucleotides on the metal surface [6,10].

Since more than one receptor is present on each nanoparticle, hundreds to thousands of nanoparticles are connected together during the hybridization process [6,10]. Nanoparticle-labeled DNA also have a sharper melting hybridization−dehybridization transition than unlabeled DNA, as a consequence of the dense loading of oligonucleotides on nanoparticle surface and of the cooperative hybridization process [13]. In this way, DNA melting temperature can be optically detected and exploited for the discrimination of different polynucleotides [6,10]. SPR assays for DNA have better target specificity and sensitivity than polymerase chain reactions (PCR). SPR assays for proteins are up to 10^6 times more sensitive than conventional protein detection methods like ELISA [6,10].

2.4 Surface-Enhanced Raman Scattering and Local Field Enhancement

The electromagnetic field in the nearby AuNPs surface is enhanced by the collective oscillation of conduction electrons [2,14]. The local field enhancement scales with particle size, and it depends strongly on the assembly of AuNPs [14,15]. The local electric field at the interstices between two AuNPs is thousands of times higher than for the same isolated particles (Figure 2(A)) [14,15]. For this reason, interparticle gaps are called hot spots, and the effect of local-field amplification on nanoscale volumes is called nanolensing [14]. The amplification increases with decreasing gap up to a plateau for a separation below about 0.5 nm, when quantum tunneling effects start compensating plasmon coupling effects [16]. Other than AuNPs multimers and aggregates, linear chains of several metal nanospheres with progressively decreasing size and separation are very efficient nanolenses [14]. The maximum field amplification is achieved within a dimer when incident light is polarized parallel to the dimer axis and for a wavelength resonant with the SPR of the dimer [14].

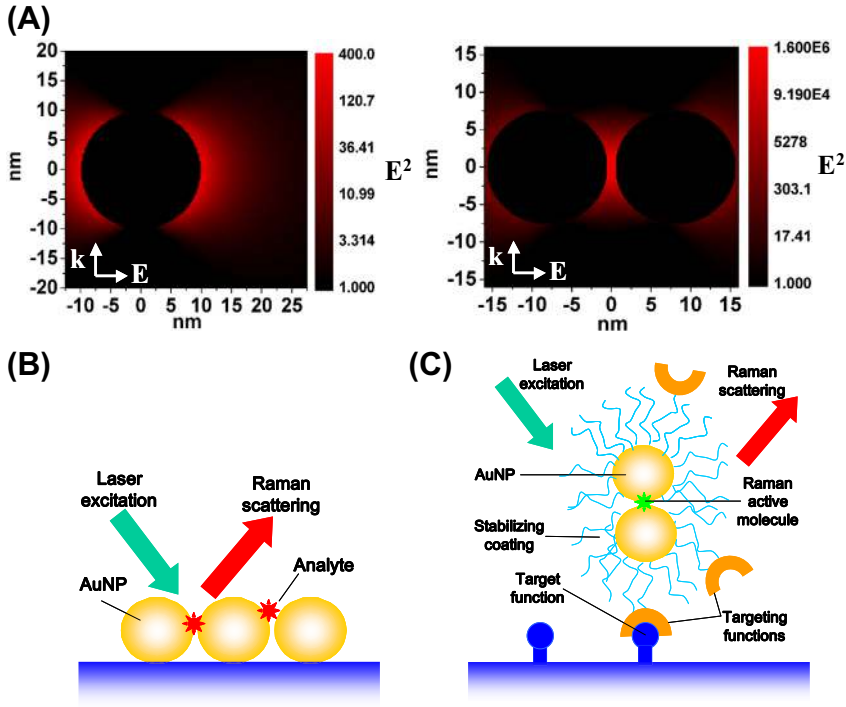

FIGURE 2 (A) The electric field is enhanced in proximity of AuNPs excited by electromagnetic wavelength. This effect is orders of magnitude higher at the junction between nanoparticles (hot spots) in particle aggregates, and this is at the base of SERS. (B–C) SERS is exploited for ultrasensitive detection of analytes by Raman spectroscopy (B) or for ultra-bright labeling of target samples (B). In (B), the analyte emits intense Raman signals when deposed on the AuNP substrate. In (C), AuNPs are loaded with a Raman-active dye and a targeting function, so that the target analyte is detected by the intense Raman signal after binding of the SERS label to the substrate.

Theoretical calculations and direct measurements on these hot spots showed that local electric field enhancement at particle interstices are useful to amplify spectroscopic signals of adsorbed organic molecules [14]. In particular, when molecules are adsorbed on metal nanoparticles or roughened metallic surfaces, a huge amplification of Raman signals is observed, called surface-enhanced Raman scattering (SERS) [14]. Enhancements up to 14 orders of magnitude for the Raman scattering cross-section have been reported [14].

When AuNPs are assembled in a way that infrared plasmon modes exist, surface-enhanced infrared absorption (SEIRA) spectroscopy is also possible [2,14].

Two distinct mechanisms can originate SERS: electromagnetic field enhancement and chemical first layer effects [2,14]. In the latter case, the electronic coupling between the molecule and the metal can produce a

resonance Raman effect due to a new metal−molecule charge transfer transition [2,14]. The magnitude of chemical enhancement has been estimated to reach no more than factors of 10−100 [2,14].

The electromagnetic field enhancement is the only one due to the localized surface plasmon [2,14], and the best conditions are obtained for molecules absorbed in hot spots, as at the junctions of metal nanoparticle homodimers [15]. It is worth to point out that the hot spot is generated by exciting the SPR with the appropriate wavelength and polarization [2,14]. Therefore, molecules in the probed volume do not contribute in the same way to the SERS signal, which is generated prevalently by the molecules located in the hot spots at the junction between plasmonic nanoparticles, corresponding to about 0.01% of the total in normal conditions [14]. This also makes the exact estimation of the enhancement factors for single molecules difficult, and a careful calibration of every substrate has to be considered for analytical purposes [14].

SERS is widely exploited for ultra-sensitive detection of analytes adsorbed on AuNPs (Figure 2(B)) [10,14]. Sensitivity of SERS is so high that single-molecule Raman spectroscopy is possible [14], as well as in vivo molecular probing of cellular components [14]. A typical application of SERS is based on the ability of Raman spectroscopy to perform multiplexed analysis [15,17,18]. The Raman spectrum is like a molecular fingerprint, and in principle, the detection of each single DNA base is also possible by SERS for a single cell [19]. In the scanometric method, AuNPs are immobilized on the chip surface by complementary base pairing when the target DNA is present [19]. Then, the reduction of silver ions on the gold particles is promoted, originating larger nanoparticles which emit stronger SERS signals [19]. Combining each base with a distinct Raman-active molecule allows the identification of the target DNA sequence [19]. Advantages of Raman with respect to ordinary fluorescence assays for DNA and protein detection are various: only one excitation wavelength is necessary, there is no photobleaching, Raman spectra have higher specificity than fluorescence spectra, and a large number of Raman-active molecules are available [6,19]. AuNPs, capped with thiol-terminated oligonucleotides composed by a Raman-active molecule on the inner end and a DNA capture sequence, have been used for the multiplexed detection of femtomolar amounts of more than six different DNA sequences in the same microarray [6,19]. The advantage of SERS, namely signal intensity, multiplexing, high signal to noise ratio, time stability, and NIR excitation, have also been exploited for in vivo biolabeling of target cells, like in cancer tissues [18]. SERS labels usually consist of AuNPs that have Raman reporters anchored to their surface, are coated with a protecting/stabilizing external layer, and are equipped with a targeting function for the selective binding of molecules like DNA, proteins, or antigens on cell membranes (Figure 2(C)) [15,17]. SERS labels endowed with antibodies showed the ability to selectively bind cancer cells and to differentiate the cancer phenotype by Raman spectroscopy [20]. SERS can be also used for the

quantification of the number of Raman-responsive AuNPs taken up by cells [17]. The proper choice of the Raman reporter and of AuNP size is crucial to enhance the SERS signal of several orders of magnitude, with best performances obtained for large particles with homogeneous size and Raman-active molecules which have absorption bands overlapped to the laser excitation wavelength [15]. When the latter case is satisfied, it is defined as surface-enhanced resonant Raman scattering (SERRS) [14]. The use of Raman-active molecules firmly bound to the AuNP surface is also an important requisite for use in the physiological environment [15,20].

2.5 Modeling of the Optical Properties

Optical properties of AuNPs can be successfully calculated by analytical and numerical models [2,5,8]. In the last 99 years, Mie theory has been successfully applied to the calculation of noble metal nanoparticles extinction cross-sections [2]. Gustav Mie solved the problem of light diffraction by a single sphere using classic electrodynamics [3]. Subsequent refinement of the theory by Stratton and Born preserved the main framework, consisting in the solution of Maxwell equations in spherical coordinates with proper boundary conditions and multipole expansion of the electromagnetic field diffused and inside the sphere [2,3]. The Mie model allows the accurate determination of AuNP concentration and average size by fitting the optical absorption spectra of nanoparticle dispersion, and a fitting program can be freely downloaded from the web to perform such calculations [4]. The core of the method consists in the calibration of the free electron relaxation frequency versus particle size with a few reference solutions of AuNPs with known average size [4]. The generalization of the Mie theory can be applied to the calculation of optical properties of complex ensembles of AuNPs, like fractal aggregates [12]. For isolated metal nanoparticles of arbitrary shape, the most widely used method is the discrete dipole approximation (DDA) [2,5,14,21]. In DDA, the nanostructure of interest is represented by a cubic array of N polarizable points, that is, N cubic dipoles [5,8,21]. There are no restrictions about the complexity or the shape of the target, the only limitation is the discrete structure of the target due to the finite number of dipoles utilized [5,8,21]. The core of DDA is characterized by the way in which the polarizability of each point dipole is expressed [5,8,21]. The most reliable formula has been developed by Draine and Goodman as a correction of the Clausius - Mossotti polarizability by a series expansion of the interdipole spacing [5,8,21]. It allows the calculation of target extinction spectra within 10% of the exact result, independently of size, shape, and particle composition, provided that the number of dipoles N is large enough [5,8,21]. For metal particles with nanometric size, an error smaller than 10% is achieved using N on the order of 40,000 [5,8,21]. Draine and Flatau developed a free code named DDSCAT, which adopts fast Fourier transform methods and complex conjugate gradient techniques to reduce the calculation time [5,8,21].

For modeling optical properties of periodic arrays of AuNPs, the finite difference time domain (FDTD) technique is often used, and it is an implementation of Maxwell's time-dependent equations for solving the temporal variation of electromagnetic waves within a finite space that contains a target of arbitrary shape, and it has recently become the state-of-the art method for solving Maxwell's equations for complex geometries [2,8,14,22]. In this method, the differentials in Maxwell's equations are replaced by finite differences to connect the electromagnetic fields in one time interval to the one in the next interval [2,8,14,22]. Because FDTD is a direct time and space solution, it offers the user a unique insight into all types of problems in electromagnetism and photonics [2,8,14,22]. It can also be used to obtain the frequency solution by exploiting Fourier transforms, thus a full range of useful quantities in addition to fields around particles can be calculated, such as the complex Poynting vector and the transmission/reflection of light [2,8,14,22]. In the FDTD technique, Maxwell's equations are discretized by using finite difference approximations in both time and space that are easy to program [2,8,14,22]. The unit cell of the lattice that constitutes the FDTD computational domain is called the Yee cell [2,8,14,22]. The advantage of this method is that results for a large frequency range can be obtained in a single run [2,8,14,22]. All the aforementioned methods rely on the appropriate correction of the optical constant of the AuNPs for size effects described in 2.2, and they allow the evaluation of the local electromagnetic field enhancement in the nearby AuNPs [2,3,8,14].

2.6 Surface Plasmon Radiative Dynamics

AuNPs have larger extinction cross-sections than organic dyes or other inorganic nanomaterials with the same size, but their luminescence is negligible [2,8,23]. Nonradiative energy relaxation processes, such as electron−electron scattering, are very fast in gold. Therefore the luminescence efficiency of AuNPs with size above 2 nm is only 10^{-5}−10^{-3} [2,8,23]. The band structure of particles with a size larger than 2 nm is almost that of bulk metals, and no quantum size effects are perceivable. The luminescence in AuNPs mainly occurs by the following three steps: the formation of holes in the lower lying *d* bands due to light absorption, the relaxation of excited electrons and holes in the *sp* and *d* bands, respectively, and the radiative recombination of the electron−hole couple [2,8,23]. The luminescence quantum yield of AuNPs can be, however, 10^{4}−10^{5} times larger than bulk gold [2,8,23]. In general, surface roughness and defects can enhance the efficiency of this process [2,8,23], as well as the surface adsorption of organic impurities with luminescence efficiency larger than the metal substrate [2,8,23]. The emission enhancement is also attributed to the surface plasmon oscillation [2,8,23]. In particular, it has been suggested that the local field enhancement due to the surface plasmon absorption can favor the radiative recombination efficiency of *sp* bands

electrons with *d* band holes, according to a phenomenon called the "lighting rod" effect [2,8,23]. The combination of high absorption cross-section, low luminescence yield and rapid relaxation of the SPR makes AuNPs attractive for applications requiring the efficient conversion of light into heat, like photothermal therapy or photothermal imaging [6,24]. Photothermal therapy offers a gentler alternative for cancer treatment by using optical heating for ablation of tumors [6,8]. Photothermal therapy requires that strong photoabsorbers are located selectively in the tumor region to reduce nonspecific injury to adjacent healthy tissue [6,8]. The absorption cross-section of AuNPs ($\sigma_{abs} \sim 2.9 \times 10^{-15}\ m^2$ for 40 nm spheres with an absorption band around 530 nm) is five orders of magnitude larger than that of indocyanine green ($\sigma_{abs} \sim 1.7 \times 10^{-20}\ m^2$ around 800 nm), a dye used in earlier demonstrations of laser photothermal tumor therapy, thus promising effective photothermal therapy at much lower irradiation energy [25]. The SPR absorption of Au nanoparticles is followed by the rapid conversion ($\sim$1 ps) of the absorbed light into heat [25]. Besides, selection of a plasmonic nanoparticle size with optimum plasmon absorption as well as scattering makes a dual imaging/therapy approach possible [25]. Therapy and imaging with visible light is suitable for in vitro studies and in vivo applications for surface-type cancers, while in vivo applications to deeper tissues require plasmon features in the near-infrared region of the spectra [25]. In general, the temperature increase due to the transformation of electromagnetic radiation into heat depends on the absorption cross-section as well as on the particle radius [24]. In particular, the temperature increase on the surface of a gold particle depends on the second power of the particle radius because of the balance between the heat generation rate, which depends on the particle volume, and the heat dissipation rate, which depends on R_{NP}^{-1} [24]. In photothermal imaging, AuNPs are heated by a laser beam, while a second weaker probe beam is exploited to locally probe the changes in refractive index due to the temperature gradient [2,8]. This technique allows monitoring very small single AuNPs (i.e., below 10 nm) inside cells [2,8].

2.7 Plasmonic Modulation of Molecular Fluorescence

Metallic nanoparticles, due to their high polarizability, show strong interactions with nearby fluorescent chromophores [26].The molecular fluorescence quantum yield can either decrease or increase depending on how nanoparticles affect the chromophore excitation rate and the radiative and nonradiative decay rates of the excited states [26]. The mechanisms of metal nanoparticle interactions with molecular chromophores can be very complicated, and several parameters govern which of the processes is predominant, like nanoparticles size and shape, molecule−nanoparticle separation and orientation, or the overlap of fluorophores excitation and emission energy with the plasmon resonance [2,8,26]. At separation distances as small as a few nanometers, quenching of

fluorescence close to 100% is observed and explained with two phenomena: the increase in *nonradiative relaxation rate* due to energy transfer from the chromophore to the metal particle and the decrease in radiative relaxation rate due to the out-of-phase oscillation of molecular dipole and the dipole induced on the metal nanoparticle, when the molecule is tangentially oriented on the metal surface [2,8,26]. The Gertsen–Nitzan model used for ordinary dipole–dipole Forster resonance energy transfer (FRET) on distances of few nm is no more valid for metal–chromophore interactions, since the theoretical d^{-6} decay is faster than experimentally observed quenching effects (d is the dipole–dipole distance) [2,8,26].

Other theories afforded the specific problem of nanomaterial surface energy transfer (NSET), like the Persson–Lang model, and were successful in reproducing the d^{-4} dependence experimentally observed [2,8,26].

Though both cases concern dipole–dipole interactions, NSET has a longer range than FRET because the nanoparticle has an isotropic distribution of possible dipole vectors on its surface to accept energy from the chromophore [26]. Relaxation of the dependence on the molecular orientation implies that NSET has a higher probability of energy transfer than FRET, is less specific of the chromophore type, and can be applied to distances over 10 nm [2,8,26]. NSET can find applications in monitoring biochemical processes, such as accurately tracking DNA length scales and conformational changes in DNA following protein binding in the distance range of 30–200 Å or structure conformational change and cleavage kinetics of hammerhead ribozyme [2,8,26].

In the presence of low quantum yield fluorophores spaced more than about 10 nm from the metal surface of nanostructures having high scattering cross-sections like AuNPs larger than 100 nm, a ten- to fiftyfold emission enhancement has been measured due to a nanolensing effect [2,8,26].

The luminescence process is particularly amplified when plasmon scattering efficiency matches the molecular emission wavelength [2,8,26]. This could be an effect of near field enhancement of the optical intensity incident on the molecule or a consequence of the increase in the photon local density of states at the emission wavelength [2,8,26]. Both effects are active for a chromophore–nanoparticle distance of 5–20 nm. Therefore, fluorescence enhancement has a distance range complementary to SERS, which involves molecules closer than 5 nm to the metal surface [2,8,26].

Conversely to fluorescence quenching, the effect of radiative rate enhancement is more pronounced and easily measurable for low quantum yield molecules [2,8,26].

2.8 Nonlinear Optics of Metal Nanoparticles

AuNPs have many highly polarizable electrons, which ensure a strong nonlinear optical (NLO) response [2,8]. Indeed, the strong nonlinear properties

of metal nanoparticles are usually attributed to local field enhancement effects for the plasmon oscillation because nonlinear optical susceptibility (χ) measured on nanostructures is much larger than in bulk metals [2,8].

Three main categories of nonlinear optical phenomena have been reported for AuNPs: optical Kerr effect, multiple harmonic generation, and optical limiting [2,8]. Except for optical limiting, the two other phenomena require pulses on the order of picoseconds or lower in order to reduce the contribution from thermal effects and nanoparticle degradation [2,8]. This is because AuNP has to be considered first of all as a converter of light into heat, especially at laser intensities typical of nonlinear optics [2,8].

Due to their enhanced third-order nonlinear susceptibility, especially near resonance with the plasmon frequency, AuNPs embedded in dielectric matrices have practical applications in ultrafast all-optical switching devices [2,8]. The switching phenomenon is based on the optical Kerr effect and consists in the intensity-dependent variation of the refractive index of the nanocomposites [2,8]. Z−scan and degenerate four-wave mixing (DFWM) experiments are used to estimate the optical Kerr susceptibility $\chi^{(3)}$ of such nanocomposites [2,8]. The magnitude of the nonlinear response varies with size and shape as well as the volume fraction of metal nanoclusters embedded in the dielectric matrix [2,8]. Three main mechanisms contribute to $\chi_m^{(3)}$ [2,8]: (1) a fast mechanism on a time scale of hundreds of femtoseconds due to electron−electron scattering after the plasmon absorption, driving to the electron thermalization, (2) a contribution from interband transition, which occurs on the same time scale of the former, and (3) a hot electron mechanism on a time scale of nanoseconds. Only the first two mechanisms are fast enough for optical switching applications [2,8].

Second harmonic generation (SHG) is possible in noncentrosymmetric systems when nanoparticle size is smaller than the excitation wavelength [2,8]. In metals, the SHG signal has two origins: a surface contribution arising from breaking the centrosymmetry at the metal surface and a bulk contribution arising from the electromagnetic field gradients due to the presence of the interface [2,8], which is the dominant contribution for nanometric particles [2,8]. Typically, SHG is observed in random metal nanostructures such as aggregated particles. Best SHG efficiency is achieved for excitation wavelengths resonant with particle SPR [2,8]. SHG is not allowed in isotropic dispersions of noncentrosymmetric particles, although a weak frequency doubling phenomenon is still possible, called hyper-Rayleigh scattering (HRS) [27]. HRS is a nonlinear second-order light scattering that has been used in the study of noncentrosymmetric molecules or nanoparticles in solutions [27]. The HRS relies upon the fluctuations of the density or orientation of nanoparticles, which instantaneously break the centrosymmetry of isotropic media as liquid solutions and create conditions of net frequency doubling [27]. Spherical metal nanoparticles functionalized with antibodies that conjugate a target antigen with a sandwich structure, forming a dimer of nanoparticles, have found

potential application in biosensing: the symmetry break upon the target antigen coordination enables the generation of HRS signal [27]. Third harmonic generation (THG) has been also reported for metal nanoparticles on a substrate, due to third order HRS mechanism [2,8]. Local field effects due to strong localization of collective plasmon modes in fractal metal clusters have been exploited for enhancing the nonlinear properties of molecules adsorbed on metal nanoparticles [2,8]. Beyond SERS effect, previously discussed, strong enhancement of HRS signal using gold nanoparticle aggregates with adsorbed pyridine molecules have been observed [2,8]. Similarly, AuNPs have been used to enhance two photon absorption-induced fluorescence for in vivo cell imaging [2,8]. AuNPs themselves are capable of multiphoton absorption-induced luminescence, with emission yield growing with particle size and asymmetry [28]. In the case of 790 nm−100 fs laser pulse excitation, the mechanism following multiphoton absorption requires that more than one photon is emitted per laser pulse and that a three photon absorption process is dominant [28]. Observed photoluminescence spectra are broad and do not show any correlation with the plasmon absorption or scattering [28].

AuNPs are well known as excellent optical limiters with nanosecond, picosecond, and femtosecond laser pulses, exploiting a mechanism not completely understood to date (Figure 3(A)) [2,8]. For the most part, investigations on metal nanoparticles pointed out the free carriers multiphoton absorption processes, the particle fragmentation due to electron photoejection, and interparticle electronic coupling in particle aggregates as possible optical limiting (OL) mechanisms [2,8,29]. Nonlinear scattering was conjectured at the origin of the strong OL in few cases [2,8,29]. Independent of the mechanism, all the investigations on optical limiting properties of AuNPs pointed

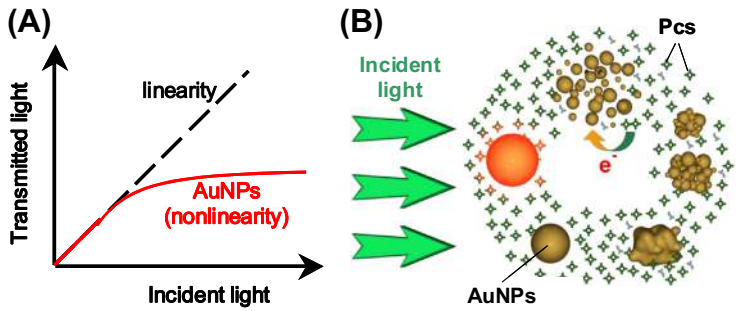

FIGURE 3 (A) AuNPs are recognized for their excellent ability to limit the intensity of transmitted light when it exceeds a critical threshold (optical limiting). (B) AuNP fragmentation, which occurs during optical limiting, can be avoided by a self-repair mechanism in the presence of phthalocyanines (Pcs), as sketched in the figure. From left in clockwise order: AuNPs absorb photons and heat up over the fragmentation threshold; electric charges are transferred to photofragmented AuNPs by the oxidation of ZnPcs, promoting particle aggregation; aggregates are photomelted into new spherical AuNPs, ready to efficiently limit light again.

out the following aspects: (1) the OL performances are amongst the best ones ever measured; (2) big nanoparticles are better optical limiters than small ones, (3) nanoparticles lose limiting efficiency after a few laser pulses due to their fragmentation, that is more rapid and has a lower threshold when particle size is big; and (4) nanoparticles have good optical limiting performances for wavelengths resonant with the surface plasmon absorption, as well as with the interband transitions [2,8,29].

In several cases, the optical limiting properties were enhanced by blending AuNPs with organic molecules, like fullerenes or β-carotene [8,29,30]. For instance, it has been reported that gold nanoparticles conjugated to a fulleropyrrolidine by a disulfur bridge showed better optical limiting performances than the isolated metal nanoparticles, with laser pulses at 532 nm (9 ns), which was compatible with an energy transfer from the AuNPs to the fullerenes of about 60% [30]. An enhancement of optical limiting has also been found for AuNPs conjugated to fullerenes−pyridine derivatives [31]. An extremely long durability under laser irradiation was observed in the case of AuNPs blended with zinc phthalocyanines (Pc) [29]. The origin of the enhanced OL performances resides in the ability of the gold nanoparticles to self-heal during the laser pulse irradiation by interaction with the Pc (Figure 3(B)) [29]. This finding is interesting because, in general, the structural instability of nanostructured materials upon their utilization can be surmounted by reducing the interface energy or by designing a nanomaterial able to self-heal or to regenerate during the usage itself [32−34]. Therefore, the AuNP−Pc blend represents a rare example of functional nanomaterials that self-heal during use [29,32−34].

3. QUANTUM CHEMISTRY OF ELECTRONIC AND OPTICAL PROPERTIES

3.1 Introduction

"First principles" calculations of gold clusters have been performed so far at ab initio level using Hartree−Fock and post-HF wave-function-based methods or with the density functional theory (DFT) approach. For gold clusters, DFT has demonstrated itself to be an excellent compromise between computational efficiency and accuracy, so it has been extensively employed in particular when the cluster size is so large as to prevent the practicability of more accurate wave-function methods. The availability of accurate quantum chemical calculations is important both to rationalize experimental results and to describe quantitatively the electronic structures of such clusters. In this respect, cluster convergence of different properties may be investigated, and conditions can be identified to locate the cluster size in order that a given property reaches its bulk value to a reasonable accuracy. In general, different physical properties are expected to exhibit different convergence behaviors

with increasing cluster size. Colloidal metals, and gold in particular, have been extensively studied with electron microscopy techniques which can find out ordered structures in nanoparticles. However, it must be considered that these colloidal metal particles are stabilized by ligand agents "coating" their surface. Although the electronic structure of stabilized nanoclusters is significantly influenced by the ligand shell, this interaction has been proven to be, in many occasions, rather confined to the top few layers at the surface of the metal cluster.

Gold exhibits strong relativistic effects, and electron correlation is known to play an important role in its compounds as well. Therefore, gold clusters are a typical field where recently developed scalar relativistic DFT methods can be successfully applied [35]. Moreover, the interest in the optical absorption of gold nanoparticles has grown in the last years, both experimentally and theoretically [36]. In fact, such systems display specific properties which make them special optical materials. This is in part due to the ability of gold to be organized in well-defined structures of nanometric size: often it is possible to tune and control the shape of such structures already at the level of a conventional chemical synthesis [37]. Therefore, it is possible to produce gold nanocluster samples with specific shape and size distributions, whose characterization is further carried on by conventional electron microscope techniques. Such samples are normally produced in solution, and gold nanoparticles are, therefore, stabilized with protective ligands: in particular, thiolates are quite popular due to their specific ability to form strong Au−S chemical bonds. Other protective agents, mainly surfactants, are also employed to stabilize nanoparticles; in this case, the gold−ligand interaction is much weaker.

The optical photoabsorption of gold nanoparticles is dominated by a strong band that, for large enough clusters, lies in the visible region [36]. This band is very sensitive to the structure of the particle and the nature of the environment: namely the size and shape of the clusters, the presence of the ligands and their nature, and finally, the solvent in which the clusters are dispersed. Such strong absorption is usually ascribed to the surface plasmon resonance (SPR) [38], and it consists of a collective excitation of the conduction electrons of the metal particle. Moreover, since SPR is a phenomenon which is localized at the surface of the nanoparticle, it is strictly connected with the finite size of the particles and, therefore, is absent in bulk material. Therefore, computational methods developed to study solid state in physics and based on periodic boundary conditions are not suitable to investigate such phenomenon. Due to the role of the SPR as a fundamental optical property of gold clusters, it has been generally considered important to develop new theoretical models with the aim of simulating this effect in order to rationalize the experimental findings and, a more ambitious goal, to perform a computational design of novel nanostructured materials with specific optical properties. In this context, the first proposed and widely used approach is the Mie

theory, whose implementations are discussed in Section 2.5 of this chapter. A first improvement beyond classical Mie theory is represented by the time-dependent local density approximation (TDLDA) implemented within the *jellium* model [39]. That is, the metal nanoparticle is modelized as a background consisting of a spherical positive charge density which describes the average nuclei positions; such a positive background supports the electrons whose motion is treated in terms of quantum mechanics. Also, in this case, the *jellium* model misses the discrete atomic structure of the cluster, but the TDLDA method gives a quantum mechanical description of the electron excitations of the model system: the SPR is described as a collective excitation of the electrons that is as free electron oscillations. Moreover, the TDLDA *jellium* model offers a practical tool to consider more specific effects which can be included in the method, namely the effect of an embedding medium to simulate, for example, the solvent effects [40]. In order to improve the theoretical description, it is, therefore, appealing to consider an approach able to retain the atomic structure of the cluster, and a possible choice would be the time-dependent density functional theory (TDDFT) formalism implemented in the conventional quantum chemical linear combination of atomic orbital (LCAO) method. This choice joins the reliability of modern TDDFT approaches to describe electron excitations with the accuracy of the LCAO implementation, which avoids the drastic approximation of the effective molecular potential operated by the *jellium* approach. Optical spectra of metal clusters protected by ligands have been calculated by the TDDFT method for many years using a finite basis set of contracted Gaussian-type orbitals [41,42] and a plane-wave basis set [43]. Of course, the LCAO-TDDFT method is computationally much more demanding than *jellium* methods. However, it represents the state-of-the-art approach for the theoretical description of the optical spectra for large molecules, and therefore, it is a potential tool to understand in detail the electron excitation process and a valid instrument to help the design of new nanoparticles with specific optical properties.

Despite the great body of experimental evidence, fundamental questions still exist in this field. In particular, there is not much unambiguous information on the dependence of the shape and peak of SPR upon nanoparticle size and shape.

3.2 Electronic Structure of Gold Clusters: Quantum Chemical Methods, Relativistic Effects, and Convergence Behavior

As outlined in the introduction, the only practical quantum chemical method to study gold clusters of large size (up to hundreds of atoms) is DFT, which consists to solve the Kohn-Sham (KS) equations:

$$H_{KS}\varphi_i = \varepsilon_i\varphi_i \tag{1}$$

The *KS* equations are Schrödinger type one-electron equations; the eigenvectors correspond to the molecular orbitals and eigenvalues to the orbital energies. The Hamiltonian of Eqn (1) has the following form:

$$H_{KS} = -\frac{1}{2}\nabla^2 - \sum_{K}^{Nucl} \frac{Z_K}{|\overline{r} - \overline{R}_K|} + \int \frac{\rho(\overline{r}')d\overline{r}'}{|\overline{r} - \overline{r}'|} + V_{XC}[\rho(\overline{r})] \tag{2}$$

In expression (2) the first term corresponds to the electron kinetic energy, the second term to the attraction between the electron and the *K*-th nucleus, the third term to the classical interelectronic repulsion, and the fourth term to the exchange-correlation potential. The electron density ρ is calculated from the occupied orbitals:

$$\rho = \sum_{i}^{occ} |\varphi_i|^2 \tag{3}$$

Since the Hamiltonian depends on the eigenvectors, Eqn (1) must be solved iteratively until self-consistency is reached. It is very important to underline the role of the exchange-correlation potential V_{XC}, a term which is approximated and, therefore, must be carefully chosen. In particular for gold clusters, it has been found that for geometry optimization, the local density approximation (LDA) is quite accurate. Whereas, for binding energies, the generalized gradient approximation is much better. In practice, the V_{XC} choice is also important according to the property of interest, in particular for photoabsorption (see Section 3.3).

From the numerical point of view, the typical quantum chemical technique of resolution of *KS* Eqn (1) consists to introduce a basis set to expand the molecular orbitals as a linear combination of atomic functions. The coefficients are then obtained by exploiting the Rayleigh-Ritz variational method. Of course, basis set size has an important impact on the accuracy of the results and on the computational effort. In the literature, various basis choices have been reported depending on the property of interest, from contracted Gaussian-type orbital (GTO) functions, for example, (19s, 15p, 10d, 6f) → (9s, 8p, 5d, 2f) to Slater-type orbitals (STO), for example, triple zeta with polarization (TZP).

A fundamental characteristic of quantum chemistry of gold compounds is the prominent role played by relativistic effects [44]. This may seem strange at first glance, since relativity should be connected with phenomena taking place around the speed of light that are far away from chemistry. Instead, relativistic effects are important for heavy atoms because the electrons of the very deep core orbitals actually move at speeds comparable to that of light. The formal treatment of relativistic quantum mechanics consists to solve the Dirac equation instead of the nonrelativistic Schrödinger equation. Although at the moment quantum chemical methods based on the Dirac equations are available, most relativistic calculations have been carried on with approximate

treatment of the relativistic effects. In fact, the Dirac equation can be approximated with proper transformations in order to reduce the dimension of the problem (from four to two or one component) [45]. Such transformations, (e.g., the Douglass−Kroll (DK) and the zeroth-order regular approximation (ZORA)) lead to a Hamiltonian, which contains most of the physics introduced by relativity and can be implemented relatively easily and applied to large systems like gold nanoclusters. In particular, three new terms are introduced by relativity: the mass-velocity, the Darwin, and the spin-orbit (SO) terms. When SO interaction is neglected, the treatment is referred to as scalar relativistic (SR). SR calculations are computationally much cheaper than SO calculations, not only because new terms must be introduced in the Hamiltonian, but also because the SO coupling reduces the symmetry. So, in practice, large systems like gold nanoclusters are usually treated at the SR level. It is worth noting that to perform accurate relativistic quantum chemistry, it is necessary to employ a relativistic basis set where the atomic functions must be optimized relativistically. On the other hand, for DFT calculations, the role of relativistic effects in the exchange-correlation functional is limited. So, it is not necessary to employ functionals obtained from the relativistic electron gas.

Despite the formalism and the computational aspects, it is interesting to describe how relativistic effects have their impact on gold chemistry. Consider first what happens to gold core *1s* and *2p* electrons, because their velocities are comparable to that of light, they are stabilized and shrunk by relativity. As a consequence, the nucleus is more efficiently shielded, and the 5*d* valence orbitals are, therefore, destabilized. The extra-stabilization of the core *1s* orbital is also reflected on the valence due to orthogonality of atomic functions. So, the 6*s* atomic orbital is stabilized as well. In summary, the 5*d*-6*s* gap of gold is more than halved in a relativistic description with respect to a nonrelativistic one. It is interesting to observe that for silver, relativistic effects are negligible, and that the Ag 4*d*-5*s* gap is comparable to the Au nonrelativistic 5*d*-6*s* gap: so silver behaves like a nonrelativistic gold. The narrowing of the 5*d*-6*s* gold gap has important consequences on the gold chemistry due to the larger involvement of the 5*d* functions in the outer valence orbitals, which makes the chemical bond more "directional." This is reflected on bond lengths, binding energies, and optical properties. Besides relativity, electron correlation is also important for gold: it has been possible to treat electron correlation by coupled cluster (CC) methods on small molecules and with perturbative Møller-Plesset (MP) on larger ones. However, for large nanoclusters, only DFT methods remain practicable.

Calculations of molecular properties of gold clusters are also important to investigate the convergence behavior with increasing cluster size. This is useful to extrapolate the bulk limit but also to identify the different roles of bulk and surface atoms.

For example, the average nearest-neighbor interatomic distance has been found to correlate linearly with average coordination number of the cluster.

So, extrapolation to the bulk limit of coordination number 12 demonstrates the high accuracy of the LDA functional to optimize the geometry [35].

On the other hand, binding energies show a linear behavior with respect to $n^{-1/3}$ where n corresponds to the number of Au atoms of the cluster: such a trend is, therefore, defined by the ratio between surface/bulk atoms, which is proportional to $n^{-1/3}$ [35].

The evolution of other properties with cluster size can also be studied, provided some simplified model is employed to identify some trend rule. For example ionization potentials (IP) and electron affinities (EA) can be studied with the spherical droplet model [46], which predicts a linearity of IP and EA with respect to the reciprocal radius of an almost spherical gold cluster. In this way, it is possible to extrapolate the experimental bulk work function of Au (5.1 eV) with excellent accuracy (4.79 and 4.86 eV for IP and EA, respectively) [35].

A complete description of the electronic structure of large gold nanoclusters in terms of molecular orbitals, although possible in principle, is not practicable due to the enormous numbers of orbitals. For this reason, the most common and convenient way to describe the electronic structure of gold nanoclusters is to employ density of states (DOS) plots.

3.3 Photoabsorption: Description of the Phenomenon, Plasmons, Size, and Shape Effects

The photoabsorption of gold clusters can by described with classical electrodynamics only for sizes larger than 20 nm, when quantum size effects become negligible, and the prominent spectral feature is the surface plasmon resonance (SPR). For a cluster size smaller than 20 nm, it becomes necessary to include quantum mechanics to describe the phenomenon. However, quantum chemistry methods are too demanding to treat particles of such size. At the moment, tridimensional-protected gold clusters up to $Au_{314}(SH)_{96}$ have been treated with TDDFT [47], which correspond to the size of the metallic core around 2.0 nm. Whereas, for bare gold nanowires with a finite cross-section, a length of 3.744 nm has been reached with Au_{122} grown along the (110) direction. [48]

There exist many different implementations of the TDDFT method for quantum chemistry; however, the most popular one is the Casida approach, which consists to solve the eigenvalue equation:

$$\Omega F_i = \omega_i^2 F_i \tag{4}$$

In Eqn (4), Ω is a matrix whose dimension corresponds to all the pairs of occupied and virtual orbitals ($N_{occ} \times N_{virt}$), ω_i are the excitation energies, and F_i are the eigenvectors from which the intensity of each excitation can be extracted. So, in practice, the solution of Eqn (4) gives the calculated photoabsorption spectrum. The elements of the Ω matrix depend upon the *KS* eigenvalues and eigenfunctions, which are calculated solving the KS Eqn (1).

So, also for TDDFT calculations, a proper and careful choice of basis set and exchange-correlation functional is important. In particular, it has been pointed out that for accurate TDDFT results, it is necessary to employ V_{xc} with correct asymptotic behavior that is supporting the Coulomb tail $-1/r$ at large distance, which is a consequence of the exchange. This characteristic is not supported by standard LDA and GGA functionals, but can be introduced with the long-range correction (LC) (e.g., in the CAM-B3LYP functional) or included in the construction of a model potential (e.g., LB94 or SAOP potentials). Basis set choice is also crucial. So, for small systems, TZP basis are usually employed. However, for large systems, the smaller and more economical double zeta (DZ) has proven accurate enough. To study the emergence of the SPR, it is convenient to consider the gold nanowire Au_{122} [17] reported in Figure 4 of this chapter: the TDDFT calculation gives a very intense band at 2.06 eV, contributed by a limited number of very intense transitions. As can be seen from the figure, at higher or lower energy, only very faint intensity is calculated. In order to assess the SPR nature of the calculated band, it is useful to compare the TDDFT spectrum (solid line) with a spectrum calculated at the KS level (dashed line) that is as dipole transition moments between occupied and virtual molecular orbitals, taking the orbital eigenvalues difference as excitation energy. From Figure 4, it is evident that while in the KS spectrum the intensity is rather uniformly distributed, in the TDDFT spectrum almost all the intensity is focused in the single band. This can be explained because the TDDFT formalism is able to describe the collective electron motion, which is the typical nature of the SPR. Whereas, the KS method cannot describe collective transitions since it is a single-particle

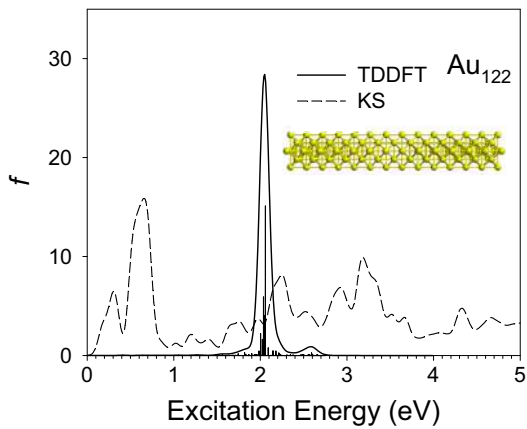

FIGURE 4 The TDDFT (full line) and KS (dashed line) photoabsorption spectra of gold nanowire Au_{122} grown along the ⟨110⟩ direction convoluted with a Gaussian function of FWHM = 0.12 eV. The vertical bars correspond to the TDDFT discrete transitions. The structure is shown in insets. *Adapted from Ref. [48], Figure 3, p. 17200.*

formalism. It is worth noting that it is very tricky to precisely identify a plasmon in a molecule. However, very recently, a systematic method based on a scalar factor has been suggested and applied successfully in a variety of different situations [49], including gold clusters. From the analysis of the effect of the longitudinal size on the optical absorption of such gold nanowires [48], it has been shown that a shortening of the nanowire induces a blue shift and an intensity reduction in the plasmon, as found in the experiment. This size effect is quite general for gold clusters and remains valid also for different shapes. Moreover, it is found that below a length of 2 nm, the plasmon disappears completely. Also, this is in good agreement with experimental findings.

In order to assess the importance of the V_{xc} choice and to identify the effect of the shape for gold clusters, in Figure 5 the analysis of a previous work of Durante is reported [50]. Four clusters are considered: (1) a cuboctahedron $[Au_{147}]^{5+}$; (2) an octahedron $[Au_{146}]^{2+}$; (3) a cube $[Au_{172}]^{4+}$; (4) an

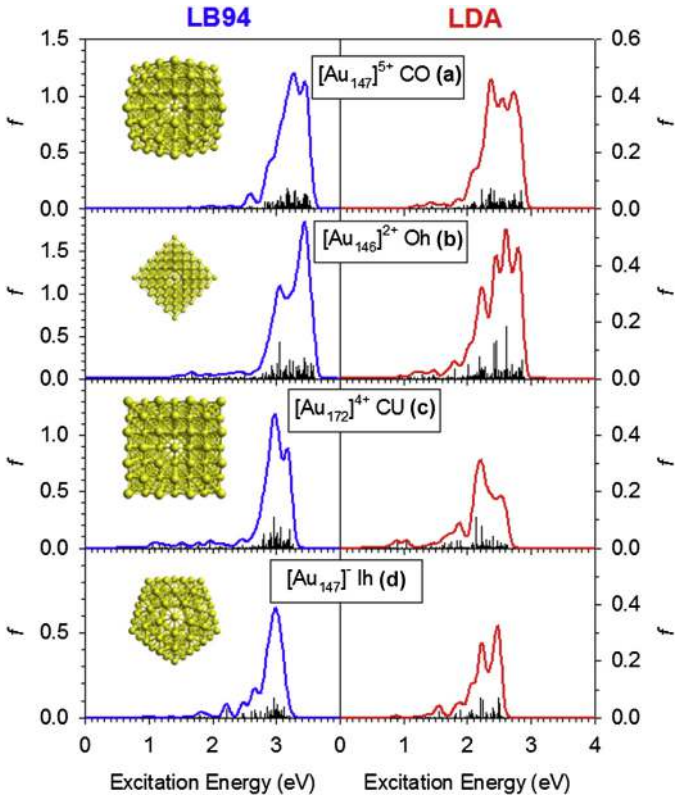

FIGURE 5 TDDFT Photoabsorption spectra calculated with LB94 and LDA potentials for Au nanoclusters. *Adapted from Ref. [50], Figure 2, p. 6280.*

icosahedron $[Au_{147}]^-$. All these structures exhibit high (O_h or I_h) point-group symmetry. (1), (2) and (3) are representative of an fcc-like (crystalline) motif, but taken with different cuts exposing only (111) facets in the case of $[Au_{146}]^{2+}$ or only (100) facets in the case of $[Au_{172}]^{4+}$, with $[Au_{147}]^{5+}$ representing an intermediate case. $[Au_{147}]^-$, instead, is representative of non-crystalline structures exhibiting fivefold symmetry axes. All these structures have been observed in actual Au nanoparticles. The charges of the clusters have been selected in order to achieve electronic shell closure. This simplification is effective in keeping symmetry high and in reducing the computational effort but hardly affects the photoabsorption spectrum.

The LB94 maximum transitions are 3.58, 3.59, 3.27, and 3.21 eV, while the LDA maximum eigenvalues are 2.88, 2.89, 2.63 and 2.55 eV for (1), (2), (3), and (4), respectively. The first and most important observation that can be drawn from an inspection of Figure 5 is that the position of the absorption peak depends weakly on the cluster shape, but it is appreciably dependent on the choice of the *xc*-functional employed in the calculations. In detail, the position of the peak maximum varies in the range from 3.0 to 3.4 eV at the LB94 level; whereas, it ranges between 2.3 and 2.6 eV at the LDA level. This provides the possibility of validating the *xc*-functional (i.e., to determine which is the most appropriate to predict the optical response of Au clusters) by comparison with available experimental data. In fact, it is known from the experiment that Au particles of roughly 2 nm diameter included in Al_2O_3 exhibit a maximum in the absorption spectrum at about 2.58 eV. This value must be corrected by the dielectric constant of Al_2O_3 and to the reduced size of the present clusters (diameter of roughly 1.7−1.8 nm). When both effects are included, one expects that the experimental peak for particles similar to those considered in Figure 5 should be around 2.9−3.0 eV. Therefore, it can be concluded that the LB94 values for the absorption maximum seem to be in better agreement with the experiment than the LDA ones. The dependence of the position of the peak on the cluster shape is instead weak. Basically, one can observe only a shift of this position to a lower binding energy by ≈ 0.2 eV at both the LDA and LB94 level for (4) and (3). The latter shift can be justified by the larger size of the (3) cluster, in agreement with the expected decrease of the position of the absorption peak with increasing cluster size. Whereas, the former shift is due to the higher symmetry of the I_h group, which narrows and reduces the number of electron−hole pairs in the excitation spectrum. The maximum of the absorption peak instead is somewhat more dependent on the cluster shape. This is due to an appreciable dependence of the *form* of the absorption onto the shape of the particle: especially at the LDA level, one can clearly see that the absorption spectrum has a roughly symmetric form for (1), and asymmetric forms for the other clusters, with a positive skewness for (2) and (4) (with the position of the maximum thus at higher energy than the centre of the peak) and negative skewness for (3) (with the position of the maximum at lower energy than the center of the peak). This is the reason for the greater sensitivity to the

cluster shape of the maximum of the absorption peak with respect to its center. In Figure 5, the sudden decline of photoabsorption peak towards high energies is the consequence of the limited number (300) of eigenvalues actually extracted from Eqn (4). In fact, when very large systems are considered, it is very hard to calculate valence photoabsorption spectra over a wide excitation energy range. In fact, the Davidson algorithm employed to diagonalize very large Ω matrices is very efficient, but it is limited to extracting a relatively small number of the lowest eigenvalues and eigenvectors. It is worth mentioning that other approaches, based on the temporal evolution, do not suffer this problem and can easily calculate the spectrum over a wide energy interval [51]. However, in such methods, it is not possible to assign the spectral features to a specific electronic transition; this makes it difficult to rationalize the calculated spectrum in terms of electronic structure. On the other hand, the Casida formulation allows for a complete analysis describing each electronic transition in terms of a linear combination of one-electron excited configurations.

In conclusion, state-of-the-art quantum chemical implementations of TDDFT have proven to be competitive to describe and rationalize photoabsorption of gold nanoclusters with sizes around 2−3 nm containing some hundreds of gold atoms. Further studies to suggest new methods and algorithms to treat even much larger systems still represent a big challenge for modern quantum chemistry.

4. QUANTIZED CHARGE TRANSFER OF NANOPARTICLE MOLECULES AND ENSEMBLES

4.1 Introduction

The size dependence of the properties of metal nanoparticles has been exemplified rather extensively, in electrochemical studies of mercapto-functionalized gold nanoparticles where the nanoparticles behave as nanoscale molecular capacitors [52]. An interesting example of these size-dependent properties is the quantized capacitance charging of gold nanoparticles that is manifested as a series of rather evenly spaced voltammetric peaks, and when the diameter of the nanoparticles is reduced to the order of the metal's Fermi wavelength (∼0.5 nm for Au), a semiconductor-like bandgap starts to emerge with a zero-current region observed in the voltammetric profiles [52].

Such quantized (single electron) charging of nanoparticles has been observed both with single nanoparticles by scanning tunneling microscopic/spectroscopic (STM/S) measurements as well as by solution electrochemical studies of nanoparticle ensembles [53]. In the former, the charge-transfer properties of a single nanoparticle (which can be an ill-defined component of nanogranular structures or a relatively well-defined, isolated metal

nanoparticle) are probed with an STM tip in a double-junction configuration [54]; whereas, in the latter, an ensemble of nanoparticles undergo charge-transfer reactions at the electrode–electrolyte interface [53]. In further studies, nanoparticle solid films have also been found to exhibit quantized charging characteristics when the nanoparticles are reasonably monodispersed in size [55,56]. In the following, we will summarize the key results of nanoparticle charge-transfer chemistry in these three structural configurations.

4.2 STM-Based Coulomb Staircase of Single Nanoparticles

Electronic devices based on simple molecules or nanostructures represent an effective and attractive solution to the grand challenge of continuing diminishment of feature size with ever-enhanced performance, a concept pioneered by Aviram and Ratner [57]. Within such a framework, nanostructures, such as organically capped nanoparticles, have been proposed to serve as the active components to achieve the diverse functionalities of device elements in manipulating electrical outputs, analogous to silicon-based semiconductor materials, by taking advantage of the ready manipulation of their structures and properties through molecular design and nanoscale engineering [58]. One fascinating characteristic is that the electronic conduction in such nanostructures can be varied from insulating to metallic by controlling the size of the nanoparticles and the strength of coupling between them [59]. For instance, when the diameter of metal nanoparticles is reduced to the order of the metal's Fermi wavelength, the phenomenon of quantized charging will appear in the nanojunction, which is commonly known as "Coulomb staircase" in STS measurements [54]. In these studies, a double barrier tunnel junction (DBTJ, Figure 6(A) and (B), reproduced with permission from Xu and Chen [60]), which consists of an STM tip, a nanoparticle, and a conducting substrate, is generally used to interpret the charge transfer properties. One

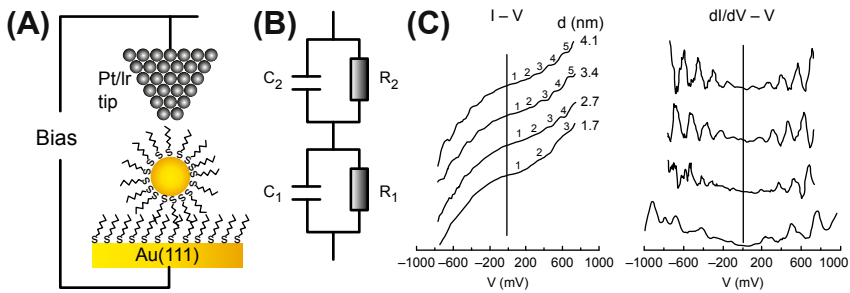

FIGURE 6 (A) Schematic of a DBTJ setup formed by an STM tip, a ligand-stabilized gold particle, and a Au substrate. (B) Corresponding equivalent circuit of the DBTJ structure. *Reproduced with permission from Ref. [60], ©2008 Elsevier B. V.* (C) *I–V* data of isolated Au nanocrystals of different sizes. The derivative spectra are shown alongside. *Reproduced with permission from Ref. [61], ©2000 Elsevier B. V.*

junction is formed between the nanoparticle and the STM tip, and the other between the metal nanoparticle and the conductive substrate.

Experimentally, Coulomb staircase is observed when two prerequisites are satisfied [52,62]. First, for an isolated metallic nanoparticle of capacitance (C), the energy associated with transferring one electron ($E_c = e^2/2C$) must exceed thermal kinetic energy (k_BT). At room temperature ($k_BT = 26$ meV), this dictates that the metal nanoparticle size must be below 10 nm so that the capacitance is on the order of 10^{-18} F. Second, the electrical contacts to the particles must have tunneling resistance larger than the quantum resistance ($h/4e^2 \sim 6.5$ kΩ), in order to suppress quantum fluctuations of the electron charge.

Coulomb blockade may also be observed. Coulomb blockade is an electronic phenomenon where the tunneling current is suppressed because the electron does not have sufficient energy to tunnel through the junctions. The origin of this phenomenon lies in the fundamental quantization of the electron charge, and it occurs in systems with small quantum charge fluctuations. As a result, the redistribution of junction charges necessarily associated with a current flow can be made only in quantized units of e. The correspondingly quantized electrostatic charging energy, which for small nanoscale junctions can be large compared to other relevant energies related to temperature and bias voltage, tends to block the current [63,64].

As aforementioned, one prerequisite for the appearance of Coulomb staircase is that the core size of the metal nanoparticle must be below 10 nm at room temperature. Indeed, particle size plays an important role in dictating the step width. Figure 6(C) depicts the conductance and corresponding differential conductance of Au nanoparticles of 1.7, 2.7, 3.4, and 4.1 nm in diameter [61]. In this range, the nanoparticles are small enough to have discrete charging energy but are above the nonmetallic regime [65]. The step width at higher bias in $I-V$ profile is Coulomb staircase, and the featureless region around the zero potential position is Coulomb blockade. The dI/dV plot shows uniformly spaced peaks that correspond to the steps in the $I-V$ curve. Both the step width and the number of steps do point to a size effect. Specifically, the number of steps increases, and the corresponding step width decreases with increasing size of the nanoparticles. The Coulomb blockade also increases with the decrease of the particle sizes, which is ascribed to the emergence of a HOMO-LUMO energy gap for ultrasmall particles [52]. Similar size-dependent behaviors have also been observed in organically passivated gold and ruthenium nanoparticles [66].

As the thermal kinetic energy (k_BT) is directly decided by the experimental temperature, the lower the temperature, the more likely Coulomb staircase becomes visible. For example, Au nanoparticles (mean size 3.5 nm) show well-defined Coulomb staircase curves at 20 K, even at high voltage bias [67]. But the features of Coulomb staircase become increasingly indistinguishable at 50 K. The tunneling current at 20 K is actually larger than that at 50 K because electron tunneling through the junction becomes more feasible at

decreasing temperature. Similar behaviors have also been reported with Pd nanoparticles [68]. Further studies show that charge transfer through the nanoparticle junctions can also be impacted by the chemical environments, which may be exploited for the development of novel chemical sensors. The sensing mechanism is based on sorption of chemical vapors into the particle organic shells and, hence, an increase of electron transfer resistance [69]. For instance, the tunneling currents of hexanethiolate-protected gold (AuC6) nanoparticles around 6 nm exhibit a rather sensitive variation upon the exposure to varied organic vapors [60]. The $I-V$ profiles show a drastic enlargement of the Coulomb gap with increasing vapor concentration and decreasing vapor relative polarity. The differences of these experimental observations can be accounted for by the effects of vapor solvation on the nanoparticle charging energy that dictates charge transport across the tip−particle−substrate junction.

4.3 Electrochemical Quantized Charging

4.3.1 Solution Electrochemistry

In electrochemical studies, analogous quantized charging behaviors have also been observed with solutions of nanoparticles of varied size and narrow dispersity. In 1997, Murray and co-workers [52] first discovered that alkanethiolate-protected gold nanoparticles in solution exhibited quantized electrochemistry that was analogous to the STM Coulomb staircase. The main difference is that in STM measurements, a single particle is probed; whereas, in electrochemical experiments, an ensemble of nanoparticles is charged and discharged at the electrode−electrolyte interface. Additionally, in contrast to the staircase features, electrochemical responses are a series of voltammetric peaks that appear to be diffusion-controlled. These voltammetric responses are ascribed to the quantized charging of the nanoscale double-layer of the particle molecules, that is, the nanoparticles behave as diffusive nanoelectrodes.

The basic premise is that the distribution of electrons between the working electrode and the nanoparticles is determined by the potential applied to the working electrode (E_{APP}), the potential of the nanoparticles (E_P), and the capacitance of the nanoparticle:

$$E_P = E_{PZC} + \frac{ze}{C_{CLU}} \tag{5}$$

where E_{PZC} is the potential of zero charge of the nanoparticle, z is the number of electronic charges on the particle (i.e., at $z > 0$, the particle is oxidized, while at $z \ll 0$, reduced), and e is the electronic charge. From Eqn (5),

$$\Delta V = E_p - E_{pzc} = \frac{ze}{C_{CLU}} \tag{6}$$

If $z = 1$, ΔV is the potential spacing between two neighboring charging peaks, from which C_{CLU} can be evaluated, and for a spherical nanoparticle coated with a uniform monolayer (of dielectric constant ε),

$$C_{CLU} = A_{CLU}\frac{\varepsilon\varepsilon_0}{r}\frac{r+d}{r} = 4\pi\varepsilon\varepsilon_0\frac{r}{d}(r+d) \tag{7}$$

where ε_0 is the permittivity of free space, A_{CLU} the surface area of the MPC core of radius r, and d the thickness of the protecting dielectric monolayer. Thus, when the core size and thickness of the organic protecting monolayer are comparable, C_{CLU} increases with increasing core radius, and for monolayers with similar dielectric property, decreases with increasing monolayer thickness.

Figure 7 shows the differential pulse voltammogram (DPV) responses of Au nanoparticles of varied size, passivated by (A) butanethiolates or (B) hexanethiolates [52]. One can see that with particles larger than 28 kDa (diameter 1.6 nm), the voltammetric charging peaks are quite evenly separated at potentials near 0 V (with a spacing of about 0.3 V). Whereas, with smaller particles, a central gap starts to emerge between the first positive and negative charging peaks. For instance, for a particle core size of 8 kDa (Au_{38}), the central gap is about 1.2 V. This is attributed to the evolution of a HOMO–LUMO energy gap due to shrinking size of the nanoparticle core, namely, a quantum size effect. These observations clearly indicate a transition of the nanoparticle quantized charging from classical double-layer charging to molecule-like redox behaviors with decreasing nanoparticle core size.

Similar responses are also observed with Au nanoparticles protected by monolayers of alkanethiolates of varied chain lengths [70]. The average full width at half maximum of a DPV peak can be as small as 115 mV, only slightly larger than that expected for a reversible one-electron process (90 mV). The corresponding nanoparticle capacitances have also been evaluated. The calculated values (Eqn (7)) are consistent with the experimental data where the monolayer thicknesses are approximated to be the fully extended chain lengths as calculated by Hyperchem®.

These electrochemical responses, the molecule-like multivalent redox behavior, of Au nanoparticles are also sensitive to the electronic interactions between the particle core and protecting ligands [71]. For two Au clusters, $Au_{11}(PPh_3)_7Cl_3$ (triphenylphosphine-stabilized Au_{11} clusters) and $Au_{11}C12$ (dedocanethiolate-protected Au_{11} clusters), both exhibit a series of quantized charging peaks, as observed previously with larger particles. In addition, the HOMO–LUMO gaps as determined from voltammetric measurements are 1.4 V for $Au_{11}(PPh_3)_7Cl_3$ and 1.8 V for $Au_{11}C_{12}$, both larger than 1.2 V for the Au_{38} particles.

More importantly, the nanoparticle electronic energy and, hence, voltammetric properties can be manipulated by simple surface chemistry because the particle core size remains virtually unchanged, and the only difference is that

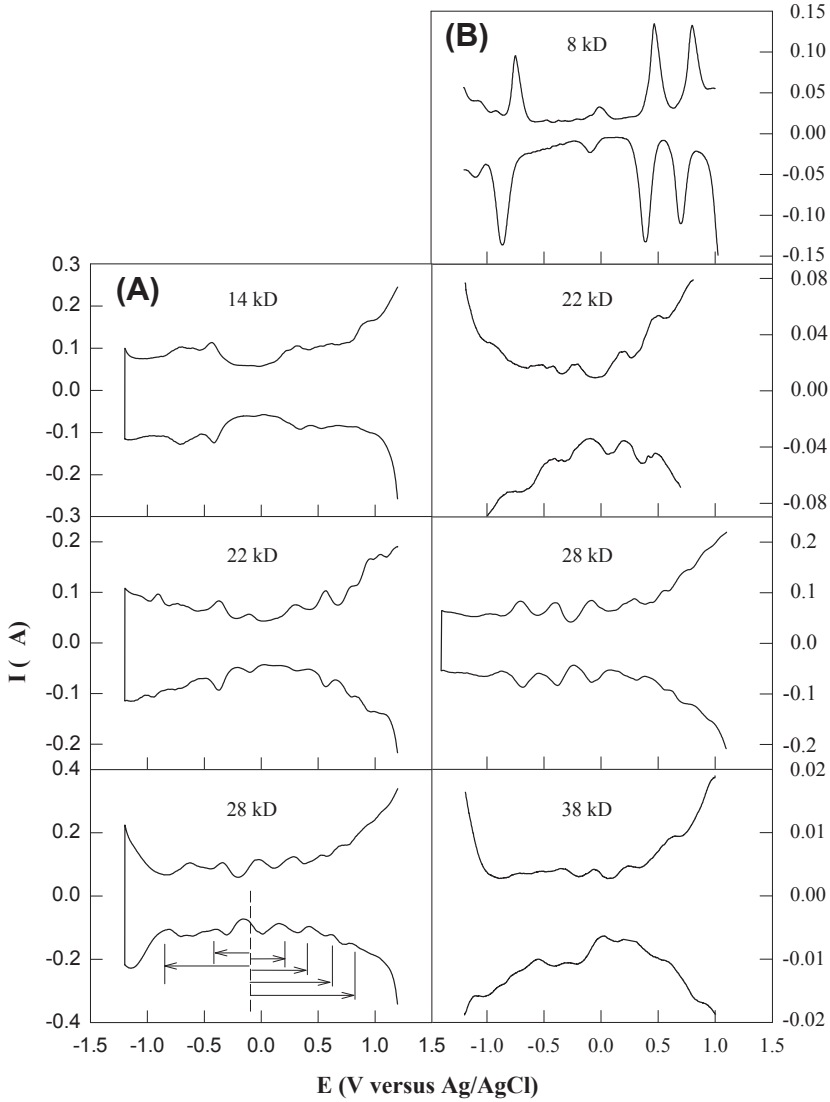

FIGURE 7 Differential pulse voltammograms for (A) butanethiolate- and (B) hexanethiolate-protected Au nanoparticles as a function of uniform core size in 0.05 M Hex_4NClO_4/toluene/acetonitrile (2/1 v:v), at 9.5 × 10-3 cm^2 Pt electrode; DC potential scan 10 mV/s, pulse amplitude 50 mV. Concentrations are: (A) 14 kD, 0.086 mM; 22 kD, 0.032 mM; 28 kD, 0.10 mM; (B) 8 kD, 0.30 mM; 22 kD, 0.10 mM; 28 kD, 0.10 mM; 38 kD, 0.10 mM. Arrows at lower left indicate ΔE potential steps. *Reproduced with permission from Ref. [52], ©1998 AAAS.*

the particle protecting monolayer is replaced from PPh_3 and Cl to dodecanethiolate (C_{12}). There are at least two areas that warrant special attention. First, the bandgap energy increases by about 0.35 V. This can be understood within the context of the stronger bonding of Au−S compared to that of Au−P (Cl), akin to the ligand-field effects on the splitting of the electronic energy of coordinated complexes [71]. Second, the Fermi level shifts positively from −0.23 V for $Au_{11}(PPh_3)_7Cl_3$ to −0.07 V for $Au_{11}C_{12}$. One possible explanation might be that the relatively weak ligand field in $Au_{11}(PPh_3)_7Cl_3$ leads to more electrons residing in the conduction band (equivalent to the high-spin state); whereas, in $Au_{11}C_{12}$, electrons are more likely to be degenerated (equivalent to the low-spin state) residing in the lower-energy valence band. Thus, the Fermi level is located at nearly halfway between the conduction band and valence band. Additionally, the electron-donating nature of P (in PPh_3) to Au is anticipated to lead to an increase of the particle core electron density and, hence, a negative (upward) shift of the Fermi level. Opposite behaviors are expected from thiol-protecting ligands, which behave as electron acceptors to gold, resulting in a decrease of the electron density of the Au cores.

4.3.2 Nanoparticle Solid Ensembles

Nanoparticle solid films are typically prepared by drop-casting/spin-casting a particle solution in a volatile organic solvent onto a flat electrode surface. The ensemble conductance has been found to be primarily driven by the thermally activated percolation effect as well as core thermal motions. Because of rampant structural inhomogeneity (disordering due to the dispersity of particle core size, shape, and chemical environments) within these particle-thick films, the energetic barriers for interparticle charge transfer most likely vary widely from site to site. Consequently, typically only featureless linear (ohmic) $I-V$ behavior is observed, especially at a relatively high voltage bias. Such disorder is one important effect for ensemble conductivity in nanoparticle solids, and the other two are the (dipolar) exchange coupling between adjacent particles and the Coulomb repulsion of electrons (of opposite spins) on a given particle [72]. In these, the disorder within the particle ensembles will diminish the interparticle electronic coupling.

Consequently, how to prepare organized and robust assemblies of nanoparticles is one of the technological challenges. An efficient surface-immobilization of nanoparticles is developed by a two-step procedure involving place−exchange reactions and self-assembly. Alkanethiolate-protected nanoparticles first undergo surface place−exchange reactions with alkanedithiols of similar chain lengths, rendering the particle surface active with varied copies of peripheral thiol groups. Excessive dithiols and displaced thiolates are removed by phase extraction using a hexane-methanol system. Self-assembling of these surface-active nanoparticles is effected by incubating the electrode in the solution, just like monomeric alkanethiols. The electrochemistry of these surface ensembles of nanoparticles can also exhibit

well-defined quantized capacitance charging features [73]. Nanoparticle assemblies fabricated on the basis of other specific interactions also show well-defined quantized charging behaviors. For instance, the cyclic voltammograms (CVs) and DPVs of nanoparticle surface ensembles by the coupling interactions between divalent metal ions and carboxylic moieties also exhibit well-defined quantized charging features. However, the peak splitting in these cases is somewhat larger than that with nanoparticles linked by alkanedithiols of similar chain lengths, implying that the nanoparticle electron transfer kinetics are impeded somewhat by the metal ion centers.

It has to be noted that the previously mentioned studies are carried out with the nanoparticle films-modified electrodes in (low-dielectric) organic media. In aqueous solutions, however, the electrochemistry of these nanoparticle assemblies is drastically different [55]. The first observation of nanoparticle electrochemical quantized charging in aqueous solutions was reported by a AuC6 self-assembled monolayer in 0.1 M NH_4PF_6 aqueous solution (Figure 8). In contrast to the behaviors in organic media, there are at least three aspects that warrant attention. First, several well-defined voltammetric peaks are found in the positive potential regime, which are ascribed to the quantized charging of nanoparticles. Second, the quantized charging features are sensitive to electrolyte composition. In the present study, the quantized charging features are only observed in the presence of PF_6^- ions but not NO_3^-. Also, the voltammetric responses do not appear to be dependent on the cationic species. Third, the voltammetric current is much larger in the positive potential regime (compared to that at the same bare electrode) but somewhat suppressed in the negative region. In essence, this behaves like a molecular diode (current rectifier). This is interpreted on the basis of the effects of the binding of hydrophobic anions like PF_6^- to the surface-confined nanoparticle molecules on interfacial double-layer capacitance. As in (low-dielectric) organic media, C_{EL} is generally smaller than C_{SAM}. Thus the double-layer charging is mainly through the surface immobilized particle molecules, which is observed at both positive and negative potentials; whereas in aqueous solutions, $C_{EL} > C_{SAM}$, the double-layer charging is generally through the naked electrode part, resulting in featureless responses only. However, in the presence of hydrophobic anions, they bind to positively charged particle molecules (at positive electrode potentials), repelling the water molecules from the interface and, hence, rendering $C_{SAM} > C_{EL}$. This ion-pairing hypothesis is further shown by the negative shift of the voltammetric profile:

$$E_f = E^o + \frac{RT}{n_a F}\ln\frac{K_2}{K_1} - (p-q)\frac{RT}{n_a F}\ln[anion] \tag{8}$$

where E_f and $E^{0'}$ are the formal potentials in the presence and absence of ion-pairing, respectively, and K_1 and q (K_2 and p) are the equilibrium constant and number of ions bound to the reduced (oxidized) form of particle molecules, respectively; other parameters have their usual significance. One can see from

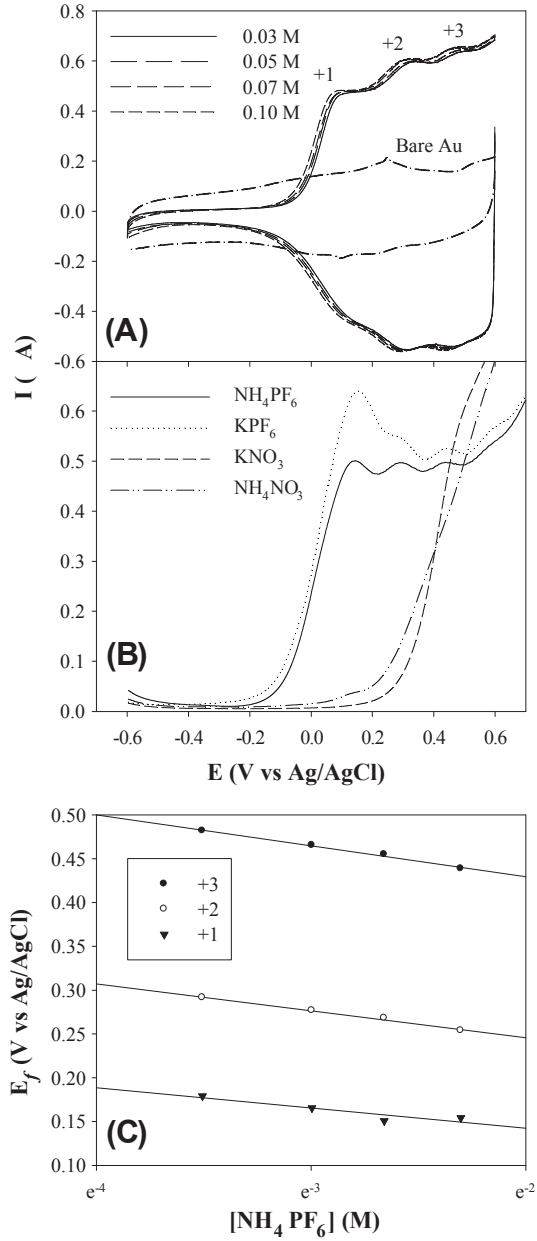

FIGURE 8 (A) CVs of a AuC6 MPC-modified Au electrode in aqueous NH_4PF_6 solutions of various concentrations. Also shown is the CV of the same bare electrode in 0.1 M NH_4PF_6. Electrode area 1.1 mm^2. Sweep rate 100 mV/s (B) DPVs of the same MPC-modified electrode in various electrolyte solutions (0.1 M). Pulse amplitude 50 mV, dc ramp 4 mV/s. (C) Variation of the formal potentials with the concentration of NH_4PF_6. Lines are linear regressions. +1, +2, and +3 refer to the three voltammetric peaks observed in (A), respectively. *Reproduced with permission from Ref. [55], ©2000 American Chemical Society.*

Figure 8(C) that all peak potentials shift negatively with increasing PF_6^- concentration, and the slopes evaluated from linear regressions are −23, −30 and −35 mV for the first, second, and third charging peaks, respectively, effectively indicating a 1:1 ratio of the number of PF_6^- ions and the MPC charge states ($n_a = 1$). It is also anticipated that the binding of anionic PF_6^- to surface MPCs increases the effective dielectric constant of the MPC-protecting monolayers, leading to the larger value of the MPC capacitance (1.05 aF).

More detailed studies involving other hydrophobic (soft) anions, such as ClO_4^- and BF_4^-, exhibit similar rectified charging features, further supporting the notion that the nanoparticle quantized charging can be manipulated by simple ion-binding chemistry. In Figure 8, one might also note that in the presence of "hard" anions (e.g., NO_3^-) the charging features are similar to those of a conventional molecular diode. At potentials more negative than the threshold value, the current is significantly suppressed; whereas at potentials more positive than the threshold potential, the current starts to increase rapidly (without the discrete charging characters). This also strongly suggests that increasing the "softness" of the electrolyte ions leads to a transition from conventional molecular diodes to single-electrode rectifiers of the nanoparticle assemblies [55].

Quantized capacitance charging has also been observed in solid-state electronic conductivity measurements of nanoparticle solid films. In these studies, Langmuir-based (LB) techniques are commonly used to fabricate monolayers and multilayers at controlled interparticle distances. The recent rapid advancement in syntheses has resulted in the ready availability of monodispersed and ultrasmall (diameter <3 nm) gold particles, rendering it possible to fabricate a clearly defined ensemble structure for the studies of their solid-state electron-transfer properties. In fact, single electron transfer can now be achieved with monolayers of these particles at controlled interparticle arrangements using the Langmuir technique. The solid-state CVs and DPVs of an LB monolayer of AuC_6 nanoparticles deposited onto an IDA electrode surface at $L = 0.72$ nm have been reported. The measurements are carried out in vacuo and at varied temperatures. When the temperature is controlled at 300 and 320 K, there are at least five pairs of well-defined and evenly spaced current peaks within the potential range of −1.0 to +1.0 V. These are, again, attributable to the single electron transfer across the nanoparticle monolayers.

4.4 Summary and Perspectives

In this section we highlighted the unique single electron transfer properties of organically capped nanoparticles. The behaviors are observed with scanning tunneling spectroscopy of single nanoparticles, electrochemical studies of nanoparticle ensembles in solution, as well as charge transfer in solid ensembles. In these studies, the nanoparticle electron transfer behaviors are

found to be directly determined by the nanoparticle size, ligand length, and interparticle separation. In addition, sensitive dependence has also been observed on the chemical environments, such as temperature, vapor atmosphere, and electrolyte ions in aqueous solutions. A good understanding of the electron transfer dynamics of such nanoscale entities is of critical importance in the further manipulation of their material properties as well as applications in the fabrication of next-generation electronic circuitries and devices.

5. MAGNETISM IN GOLD NANOPARTICLES

5.1 Introduction

The observation of ferromagnetic-like response in nanoparticles (NPs) of traditionally nonmagnetic metallic systems as Pd, Pt, Ag, and Au has motivated a great interest, as well as theoretical effort, to find its possible origin. In all cases, paramagnetic and diamagnetic in bulk materials, two challenges arise: first the origin of the atomic magnetic moments and second, the origin of the ferromagnetic-like behavior. Magnetic phenomena are strongly dependent on the changes that occur at the nanoscale, arising either from the so-called size effects, associated to the geometric confinement of electrons or from the surface effects, due to the large fraction of surface atoms since both of them modify the electronic structure of the systems. The continuum that describes the band of allowed energy states for a metal becomes a discrete set of states for NPs. In addition, the density of states at the Fermi level, the parameter that governs electronic properties, is strongly affected by the nanoscale. Some of the novel properties/phenomena that appear/occur at the nanoscale are monodomain configuration instead of a multidomain configuration, superparamagnetism, surface anisotropy, and discontinuity in the short-range order at the surface, weakening of the exchange interactions, narrowing of the bands, and enhancement of the local density of states as well as of the local magnetic moments.

Surface modification of the NPs by capping with appropriate molecules could also drastically affect the magnetic behavior of the NPs with respect to the observed behavior in bulk. In bulk solids, the dependence of physical properties on the chemical environment can be defined as weak when compared to that exerted on NPs. At the nanoscale, physical properties (e.g., optical and magnetic properties) can be tuned by using a suitable coating. In other words, the electronic structure, which is extremely sensitive to the nanoscale, will also be deeply modified by the chemical bonding of the atoms.

One of the most surprising examples of such novel magnetic properties is the observation of a ferromagnetic-like behavior in materials that are not ferromagnetic in bulk. Ferromagnetism has been observed in Pd and Pt nanostructures, typical paramagnetic materials in bulk, with a particle size below 2 nm [74,75]. More surprising is the case of noble metal Au and Ag nanostructures that are diamagnetic in bulk [76,77]. The local enhancement of

the density of states seems to be responsible for the observed behavior in Pd and Pt; whereas, an appropriate coating and the associated charge transfer is the origin of the magnetic behavior observed in Au and Ag nanoparticles. This work will focus on the magnetic behavior observed in gold nanostructures. It should be mentioned that the observation of ferromagnetism in Au NPs adds an important new functionality to this nanoscale system that, besides being magnetic or not, exhibits a broad potential in biology, catalysis, and nanotechnology. The main results obtained from the experimental magnetic characterization of Au NPs stabilized with different protective agents will be presented. Also, results obtained by element selective techniques, X-ray magnetic circular dichroism, and ^{197}Au Mössbauer spectroscopy will be summarized. Finally, a model for explaining several key features of the experimental results will be presented.

5.2 Experimental Studies

The first experimental work on a magnetic behavior different that a diamagnetic one in Au NPs dates back to 1999. Hori et al. [78] reported unexpected large magnetic moments in Pd and Au nanoparticles with particle size below 3 nm and embedded in poly(*N*-vinyl-2-pyrrolidone) at low temperatures.

These results were quite interesting since bulk Au behaves as a diamagnetic metal with a negative susceptibility of -1.42×10^{-7} *emu/g Oe*. The Au atomic electronic configuration is $[Xe]4f^{14}5d^{10}6s^{1}$. The 5*d* electrons are buried a few electron-volts below the Fermi level and the density of states at the Fermi level, $g(\varepsilon_F) = 0.29\ eV^{-1}atom^{-1}$, is very low. The occupancy of the 5*d* band can be obtained by using X-ray absorption near-edge structure (XANES) spectroscopy. By carrying out experiments at the Au L_2 and L_3 edges, it is possible to determine the density of unoccupied 5*d* states (i.e., the number of holes in the 5*d* band) since it is directly proportional to the intensity of the white line transitions (corresponding to $2p_{1/2} \rightarrow 5d_{3/2}$ and $2p_{3/2} \rightarrow 5d_{3/2,5/2}$ dipole transitions, respectively). For bulk gold, low intensities of the white line arising from a small population of 5*d* holes resulting from *s-p-d* hybridization are measured. Neglecting such small hybridization, the 5*d* band is nominally full with a balanced number of electrons in the spin-up and spin-down subbands.

Later, Crespo et al. [76] reported on the observation of an even more surprising magnetic behavior regarding magnetic hysteresis up to room temperature in 1.4 nm thiol-capped Au nanoparticles obtained by the Brust method [79]. These NPs were stabilized with dodecanethiol $CH_3{-}(CH_2)_{11}{-}SH$ that strongly bonds to the surface of the nanoparticle through the S atom. The unexpected magnetic behavior was compared with that obtained in Au nanoparticles that were stabilized by means of a tetraoctylammonium bromide $(C_8H_{17})_4N^+Br^-$, a weakly interacting and non-surface-binding surfactant. In this case, the experimentally observed behavior is diamagnetic (as in bulk gold) and anhysteretic.

The ferromagnetic-like behavior was also observed in thiol-capped Au glyconanoparticles (GNPs) where the Au nanoparticles were functionalized with thiol-derivatized maltose and lactose neoglycoconjugates [80]. In contrast with the thermal dependence of the ferromagnetic materials, almost no variation of the magnetization up to room temperature was observed in the thermal dependence of the magnetization; whereas, hysteresis was also observed up to room temperature. As in the previous work by Crespo et al., the neoglycoconjugates were bonded to the Au surface via an S atom.

It should be mentioned that elemental chemical analysis was carried out by means of inductively coupled plasma (ICP) analysis in order to estimate the amount of ferromagnetic impurities. It was observed that the low level of impurities could not account for the magnetization values.

Figure 9 shows an example of the magnetization curves exhibited by Au nanoparticles capped with thiol-derivatized molecules, as well as the one stabilized with the surfactant. The characteristic features of a ferromagnetic material, a hysteretic behavior with a coercive field and permanent magnetization even in a zero applied field, are clearly seen up to room temperature. Curves corresponding to nanoparticle-stabilized tetraoctylammonium bromide are also shown.

These results were analyzed on the basis of the results obtained by Zhang and Sham [81a,b]. By means of X-ray absorption near-edge structure

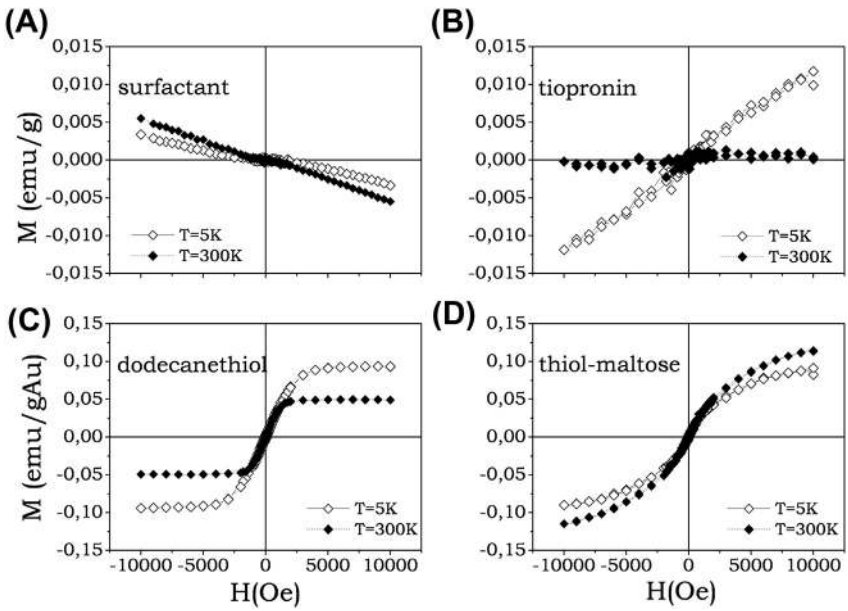

FIGURE 9 Magnetization curves at 5 and 300 K of Au nanoparticles stabilized by (A) tetraoctylammonium bromide; (B) tiopronin; (C) dodecanethiol; and (D) thiol-derivatized maltose.

(XANES) studies carried out at the *Au* $L_{3,2}$− edge, the influence of the capping system on the electronic structure of Au nanoparticles was pointed out. Au atoms in the NPs gain 5*d* electrons (relative to the bulk) when particles are capped with weakly interacting dendrimers; whereas, they lose 5*d* electrons when capped with a strongly interacting thiol molecule. This indicates that more holes are present on the gold atoms of thiol-capped particles, compared to the bulk, as a result of the Au to S charge redistribution promoted by appropriated capping. X-ray photoelectron spectroscopy corroborates this behavior. XANES studies carried out by Crespo et al. on thiol-capped Au nanoparticles showed the charge transfer from gold to sulfur atoms was extremely large in the thiol-capped Au NP; whereas, tetraalkylammonium-protected NPs exhibit a density of 5*d* holes, similar to that from bulk gold.

These changes in the electronic properties of the NPs were further studied by means of surface plasmon resonance by Crespo et al. When illuminated with light of the resonant frequency, the free electrons of the nanoparticle exhibit a collective coherent oscillation called surface plasmon resonance. The position and width of the resonance depend on the particle size, shape, as well as on the medium in which it is embedded, among other factors. The thiol-coated nanoparticles do not present surface plasmon resonance, while this feature is clearly observed for the ammonium-coated nanoparticles. This behavior was analyzed by García et al. [82] as a consequence of a decrease of the effective size of the metallic core, where conduction electrons could oscillate due to the surface localization of conduction electrons. Strong charge transfer (such as what occurs when thiols are surface-bound) localizes surface electrons, thereby broadening the surface plasmon resonance peak. For enough small particles with strongly bound thiols, this surface shell of localized electrons can become comparable or equal to the total radius of the nanoparticle, and surface plasmon resonance is suppressed due to the localized character of the electronic charges. An expression that takes into account that the region where electrons can oscillate freely could be reduced by the chemical interface damping due to the Au−S bond can be found in [82].

Thus, the ferromagnetic-like behavior of very small thiol-capped gold NPs points out that thiol bonding induces in Au NPs not only hole localization, but also permanent magnetic moments associated with the spin of extra d holes localized near the Au−S bonds. This, in combination with the strong spin-orbit coupling of Au, seems to be the origin of the observed behavior.

Following the experimental observation of magnetism in Au thin films coated with SAMs organized in ordered domains [83], the idea that orbital contribution to magnetic moment should not be ruled out, and the influence of the tendency to self-assembly of molecules at the Au surface on the magnetic behavior was investigated by Guerrero et al. [84]. Two different thiol-containing molecules with different spatial configurations were used as capping molecules of Au nanoparticles. A tiopronin-protected gold NP was synthesized, and its magnetic behavior was compared with that of

dodecanethiol-capped Au NPs. Despite Au−S bonds being present in dodecanethiol- and tiopronin-capped Au NPs, the magnetic behavior was quite different. The magnetization of the tiopronin-capped NPs exhibits a paramagnetic response at five and at 300 K, which indicates that the spins induced through binding to S atoms fluctuate in orientation, and no permanent magnetic moment is observed, see Figure 9. Whereas, dodecanethiol molecules are well known to self-assemble, and this that could induce the formation of domains in which well-ordered molecules are bonded to the surface; the self-organization of tiopronin is not a straightforward issue due to the geometry of the molecule. Thus, the spatial arrangement of molecules also plays a role on magnetic behavior.

The metallic character of the nanoparticle should also be taken into consideration. As mentioned previously, the magnetism observed in the thiol-capped NPs was found to be accompanied by a partial suppression of the plasmon absorption, indicating that the itinerancy of the 5*d* electrons of Au was partially inhibited due to the strong interaction between the thiolate and the surface gold atoms. Two set of samples were prepared: a Au-thiol (polymeric) phase and the well-known dodecanethiol-capped Au NPs. XANES confirmed the formation of a −Au−S−Au−S− polymeric network without Au−Au metallic bonds for the Au-thiol (polymeric) phase. However, the number of Au−S bonds in the polymeric phase was greatly enhanced when compared with dodecanethiol-capped NP; a diamagnetic behavior was observed [85].

Thus, it was experimentally shown that the presence of a ferromagnetic-like behavior is associated with the formation of NPs with simultaneous presence of Au−Au (metallic character of the nanoparticle) and Au−S bonds, as well as with the tendency of thiol-derivatized molecules to form ordered domains. As will be discussed later, this result indicates that the contribution of orbital magnetism due to conduction electrons should be taken in consideration for explaining the magnetic behavior. The formation of domains at the surface acts as a potential barrier where quasifree electrons become trapped, leading to orbital momentum induced at the surface conduction electrons. The spin−orbit coupling at Au surfaces creates a strong anisotropy that could account for the magnetic hysteresis observed even at room temperature.

Before going into the details of the possible origin of the anisotropy in these nanoparticles, an important point should be clarified. When dealing with nanoparticles, one can argue whether the observed magnetic behavior, typically measured with a highly sensitive SQUID magnetometer, is intrinsic to the nanoparticle or arises from impurities of iron or its oxides. In most works, elemental chemical analysis is carried out by means of inductively coupled plasma (ICP) analysis in order to estimate the amount of ferromagnetic impurities. The level of ferromagnetic impurities found was, in all cases, too low to account for the obtained magnetization values.

Au(Fe) glyconanoparticles (GNPs) with particle sizes below 2 nm were prepared by introducing a controlled amount of Fe impurities by a one-step synthesis developed by Penades et al. [86] for studying the effects of impurities on the magnetic behavior of Au nanoparticles. The Fe content of the samples ranged between 0.06 wt% Fe and 2.8 wt% Fe. Surprisingly, it was observed that the spontaneous magnetization of AuFe GNPs exhibited a fast decrease with temperature that contrasted with the almost constant value of the magnetization observed in Au NPs. In addition, no ferromagnetic-like behavior was observed at room temperature. It seems reasonable not to ascribe the amazing ferromagnetism exhibited by Au NPs with the presence of magnetic impurities since the presence of Fe clearly weakened the magnetic behavior [76].

However, to evidence that the magnetism is intrinsic to the nanoparticles, element selective techniques such X-ray magnetic circular dichroism (XMCD) and Mössbauer spectroscopy should be used. XMCD is a powerful technique that consists of measuring $L_{2,3}$ absorption edges using circularly polarized X-ray photons in the presence of a magnetic field which is applied along and against the X-ray photon's momentum. The difference between the two XANES spectra yields the XMCD spectrum, which allows determining the difference between spin-up and spin-down densities of states. Furthermore, the technique allows us to separate the spin and orbital contribution to the magnetic moment.

The first experimental evidence by XMCD of a magnetic moment on gold was provided by Yamamoto et al. on PAAHC−Au nanoparticles [87]. This study confirmed that Au atoms are bearing a magnetic moment. Garitaonandia et al. [77] have combined XMCD measurements with ^{197}Au Mössbauer spectroscopy for determining the origin of the magnetization in thiol-capped Au NPs. The field dependence of the magnetization extracted from XMCD data shows a clear hysteresis, similar to that observed by SQUID magnetometry. Moreover, in the Mössbauer spectrum performed at low temperatures, 4.2 K, two contributions were observed, one arising from the core gold atoms and a second contribution that consists of a magnetically split signal attributed to the surface gold atoms. Their results demonstrate that the magnetization in thiol-capped Au NPs is localized in the 5*d* orbital of Au atoms. Although the values of the magnetic moment per Au atom, $0.3\mu_B$, were higher than those reported by others, the main conclusion of this study is that it is clearly proved that the gold atoms in the nanoparticle surface are carriers of the magnetic moment. Later, de la Venta et al. [88] conducted a similar study on thiol-capped Au nanoparticles (NPs) embedded into polyethylene. Their results also showed that show that the magnetism observed in thiol-capped Au NPS is a magnetism that is intrinsic to the nanoparticle, and it cannot be attributed to *para*- or ferro-magnetic impurities.

Ferromagnetism has not only observed in Au NPs capped with thiol-derivatized molecules. Hori et al. [89] have also reported ferromagnetic

behavior in Au NPs stabilized with polyacrylonitrile and polyallyl amine hydrochloride (PAAHC). Ferromagnetic spin polarization of Au nanoparticles protected by PAAHC with a mean diameter of 1.9 nm was measured by XMCD. Au nanoparticles coated with oleic acid and oleylamine with sizes below 7 nm and a narrow size distribution were also reported to exhibited ferromagnetic behavior [90]. More recently, ferromagnetic-like behavior has been also observed in phosphine-capped Au NPs [91a,b] and thiolated azobenzenes [92].

5.3 Origin of the Magnetic Moment

Since gold NPs dispersed by a surfactant are diamagnetic, the ferromagnetic-like behavior observed for thiol-capped Au NPs must be associated with the modification introduced in the Au electronic structure by the Au−S bond. This result indicates that the origin of the magnetic behavior lies in the different degree of interaction between Au atoms and the protective molecule. Therefore, and as clearly derived from a broad spectrum of experimental reports, the unexpected characteristics of the magnetic behavior of nanoparticles of materials that are far from being magnetic in bulk, as is the case for Au, are mainly conditioned by the capping molecules. The bonding nature between these molecules and the surface atoms of the NPs determines the modification of the electronic structure of the surface that leads to the appearance of the unexpected magnetic moment.

In order to undertake a study of the intrinsic origin of the magnetization in gold nanoparticles, a more detailed understanding of the nature of the gold−alkanethiol bond is, therefore, required. In particular, understanding of the interaction between the capping molecules as alkanethiols and Au NPs is currently one of the main challenges in the study of their magnetic structure. Several articles related to the sulfur atom bonding with Au clusters have been published.

Recent ab initio calculations show that the S−Au bond is such that an electron is transferred to the Au cluster [93]. Therefore, the appearance of the magnetic moment in Au was always associated with either electrons or holes transferred from the capping molecules.

In the next paragraph, the main theoretical efforts oriented to account for the induction of the magnetic moment are outlined.

A second challenge is to account for the room-temperature hysteresis loop observed in Au NPs. In general, the presence of hysteresis in the magnetization curve of a sample indicates that the atomic magnetic moments are coupled to each other through exchange interactions. In fact, hysteresis is due to magnetic anisotropy rather than to exchange interactions. In ferromagnetic NPs as small as 1.4 nm in diameter, the expected behavior at room temperature is superparamagnetic, provided the usual values of anisotropy hold. For instance, Fe NPs are blocked if their diameters are larger than 30 nm. Then the question is:

what is the strength and origin of giant anisotropy that forces a 6 nm diameter Fe (or Au) NP to remain blocked at room temperature? Different proposals have been made in order to explain the hysteresis of the NPs. Vager et al. [94] suggested that the applied magnetic field would induce a giant paramagnetic moment on those electrons involved in the bonding to the capping molecules. The high magnetic anisotropy suggests that some kind of orbital contribution to the magnetic moment cannot be disregarded. Following this suggestion, Hernando et al. proposed a model including orbital magnetism. This model [95–97] assumes the induction of orbital magnetism by motion of surface electrons around ordered arrays of Au–S bonds.

5.4 First Principle Calculations

Theory and experiments have shown that the coverage of magic gold clusters by thiols of well-defined compositions is rather complicated [98]. Sulfur atoms are attached with a single bond to a gold atom of the cluster [99,100]. These magic or closed-shell clusters are highly ordered arrangements with full electronic sp shells, as in noble metal clusters in general [101]. Furthermore, alkanethiols with longer chains on Au surfaces have been the focus of detailed theoretical studies [102], and the presence of several different metastable states is known. In these cases, the sulfur atoms in the gold layers become arranged in a bridge configuration for the ground state.

The experimental findings in capped Au NPs are now supported by theoretical total energy calculations. Gonzalez et al. [103], based on the results of thiol-capped Au NPs, presented a simple model that addresses the induction of magnetic behavior in gold clusters on chemisorptions of one organic molecule with different chemical linkers (nitrogen and sulfur linkers). The system under consideration was a small cluster of 13 gold atoms and one chemisorbed molecule. It was found that the interaction between the S and Au orbitals was ultimately responsible for the onset of magnetism in thiol-capped gold nanoclusters, in agreement with the proposal of Crespo et al. [76]. This model showed that for a sulfur linker, energetic stabilization is accompanied by the development of spin localization preferentially in the gold atoms closest to the chemisorption site. Whereas, for a nitrogen linker, no spin symmetry-breaking leading to lower energy states is found. Later, different theoretical models have reported size-dependent magnetization and spin symmetry-breaking that would explain the experimental results found for thiol-capped gold and silver NPs [104,105].

It is now well established that the contribution of the sp levels in Au NPs is, rather than the *d*-ones, particularly significant, and it is the filling of these levels that explains the effects of the electronic shells in noble metal clusters, in general, and in gold clusters, in particular. In particular, first principle calculations point out that the S–Au bond is such that sulfur does not get a charge, and an electron is transferred to the Au cluster [93,106].

Alkanethiols with longer chains on Au surfaces have been the focus of detailed theoretical studies [102], and it was shown that there exist different metastable states in energy. The sulfur atoms in the gold layers becomes arranged in a bridge configuration for the ground state, and this must then be primarily considered in assessing their magnetic signal.

The ADF (Amsterdam Density Functional) method [107] was used for calculations involving density-functional-theory (DFT). The valence basis set was composed of the *d* gold, sulfur, carbon, and hydrogen states, which were expanded in triple zeta with two polarization functions at each atom. The relativistic effects of gold were modelled using the zeroth-order regular approximation (ZORA) [108], and its scalar relativistic version was implemented for the structural optimizations.

We carried out a study [106] with a cluster of Au_3, which allowed us to investigate a number of different coordination numbers for the sulfur atom. Au_3SCH_3 has an even number of electrons and thus has a spin moment equivalent to an even number of Bohr magnetons. The data were obtained using generalized gradient density approximations (GGA) with the parameterized exchange-correlation functional of Perdew−Burke−Ernzerhof according to [109]. The optimization of the geometry was carried out until the forces were all smaller than 0.02 eV/Å. The magnetic anisotropy (MAE) was obtained by means of self-consistent ZORA relativistic calculations, including spin-orbit. It was found that the singly or doubly occupied levels of the Au clusters are responsible for the odd-even oscillations of the magnetic moment located at the Au atom participating in the sulfur bonding.

Our calculations predict that the bonding of alkanethiols on gold clusters (i.e., Au_nSCH_3) results in a bridge arrangement with a deviated axis in a polarized ground state for even values of n. For this structure, the sulfur atom and the close pair of atoms are responsible for the chemical bonding, but it is the outer gold atoms that host the larger part of the magnetic moment. The large magnetic moment is preserved in the structure of the nanoparticles because they have lower symmetries. Thus, it should be possible for the particles of other noble metals to show similar magnetic behavior.

There are five sulfur electrons in total: the two bonds with gold atoms share two electrons, an electron is shared in the bond with the carbon atom, and two more form the lone pair in the sp^3 hybridization. Because each sulfur atom contributes a total of six electrons, a single electron is left over and is passed to the gold cluster. It is this sp electron that contributes to the spin polarization.

A related discussion that supports the back-donation of a sp electron from the sulfur to gold arises from a comparison between the electronegativity of thiols and that of their gold counterparts. We calculated the ionization potentials (IPs) and electro-affinity (EAs), thereby obtaining the Mulliken electronegativity $M = (IP + EA)/2$. This M value is the negative of the electrochemical potential. The electronegativity of the SCH_3 unit is slightly higher (5.43 eV) than the work function ($\approx$5.22 eV) for the Au surface [110]

and is comparable with the M value for gold nanostructures (<6 eV) [111]. The SCH_3 unit behaves rather differently from the sulfur atom ($M = 6.21$ eV). In consequence, the transfer of charge from gold to sulfur cannot be assumed a priori. In fact, we stress that independently of the used partition scheme, the calculated transfer of charge between the thiols and the gold clusters is less than 0.1 e.

Our findings point out a gain in energy of 0.12 eV for the $-SCH_3$ adsorbate with the gold cluster in a bridge position, this being the ground-state structure with respect to the molecule in the Au_3 plane. The most important characteristic is the shift between odd-even oscillations by a single gold atom with respect to bare gold clusters. The structure is spin compensated for an even number of gold atoms in the thiol-cluster, while it is spin polarized otherwise.

It must be stressed that the sulfur atom is not negatively charged, even though XANES experiments have shown that the 5*d* orbitals of gold are slightly open. The sp contribution to the magnetic signal is larger than that of the d orbitals. The back-donated electron from sulfur to gold also sits in the sp states of the Au bond and cannot be differentiated from the previous results using the XANES method. These sp electrons are almost free in the second gold layer and could orbit, and it is these that are responsible for the magnetism. As shown in the next paragraph, these findings are consistent with experimental results in which a number of gold layers are needed in order to engender thiol-induced magnetism.

By including spin-orbit coupling, we find that thiols attached on Au_4 and Au_6 show magnetic anisotropies, MAE, of 1.43 and 0.98 meV per SCH_3 molecule, respectively, while the change of MAE in the plane parallel to the surface is less than an order of magnitude smaller. These figures are comparable with the giant magnetic anisotropy of single cobalt atoms on a Pt surface (9 meV per Co atom) [112]. Such large values of MAE demonstrate the stability of the magnetism discussed herein at room temperature and are a factor of 10 times larger than the equivalent values for tetragonal Ni (0.2 meV). The experimental results, outlined above, showed that the magnetism of gold nanoparticles covered by thiols can indeed survive almost unchanged at room temperature.

5.5 Magnetic Moment of an Electron Gas Confined on a Spherical Surface

In order to estimate the permanent magnetic moment of the electrons occupying the 4sp surface states, we must begin by calculating its energy spectrum and eigenstates. Let us initially consilder that the electrons donated by the capping organic molecules are confined by a Dirac δ potential to jump between surface atomic sites, thus forming an electron gas depicted by its effective mass. In the following paragraph, it will be shown how the unfilled surface layer gives rise to a permanent collective magnetic moment. Let us summarize the more important features of the energy spectrum of an electron gas confined

on a spherical surface. The corresponding eigenstates of a noninteracting gas confined in the spherical surface of NPs [113–117] are the spherical harmonics $U_{l,m}(\theta,\varphi)$, and their associated kinetic energy eigenvalues depend on the angular quantum number l as

$$e_l = \frac{l(l+1)\hbar^2}{2mr^2} = \frac{l(l+1)}{2}e_1 \tag{9}$$

where r is the radius of the NPs, and m is the effective mass of the electron that can be written as $m = \frac{\hbar^2}{2a^2b}$, b being the hopping amplitude proportional to the surface band width ($\approx 4b \approx 4b$) and a is the average interatomic distance at the surface. Notice that $e_l = \frac{\hbar^2}{mr}$.

Let N be the number of surface atoms available to supply an electron through a bond to the capping molecule and suppose that each bonding supplies an extra electron. There are actually $N_b = \alpha N \ll \mathrm{N}$ electrons, where the coverage factor $a \ll 1$. If we proceed by filling successively the levels of increasing energy given by Eqn (9) up to N_b, and after taking into account that the maximum number of electrons that can occupy any level is given by $2(2l+1)$, it can be seen that the Fermi level, l_F, is implicitly defined through the following relationship [118].

$$N_b = \alpha 4\pi\left(\frac{r}{a}\right)^2 = 2(l_F+1)^2 \tag{10}$$

From Eqn (9) and Eqn (10), the distance in energy between the Fermi level and the level immediately above, Δ, can be expressed as

$$\Delta = 2b\sqrt{2\pi\alpha}\ \frac{a}{r} \tag{11}$$

The experimentally measured width, $4b$, of surface bands varies between 0.5 and 1.0 eV [119]. Therefore, for $b = 0.25$ eV and $\alpha = 1$, Δ is given approximately by $\left(\frac{a}{r}\right)$ eV. Consequently, for $\left(\frac{a}{r}\right) > 0.023$, the distance Δ should be larger than the thermal energy at room temperature, and the transition induced by scattering to upper energy levels (upper l values) may be disregarded. For $\Delta > 0.3$ eV, the excitation of electrons to levels above the Fermi level induced by either exchange interactions or an applied magnetic field should then be negligible.

The distance Δ remains larger than the thermal energy for the sufficiently small size of the NPs. As the size of the NPs increase, the distance between adjacent levels decreases and the surface band energy spectrum approach to a continuum. It is also observed that for a given NPs size, the discreteness of the spectrum increases with the hopping term b, as is obviously expected since the increase of the hopping implies an increase of the band width keeping constant the number of levels and the coverage factor. In fact, the discreteness of the spectrum, as predicted by Eqn (11), is roughly given by the band width times the Fermi quantum number l_F.

In general, the Fermi level will not be completely filled. Let n^* be the number of electrons that occupy the Fermi level of the NP. It is useful to classify the NPs into two types, diamagnetic NPs for which $n^* = 2(2l_F + 1)$ and paramagnetic NPs for which $n^* \ll 2(2l_F + 1)$.

Associated with the n^* electrons occupying the unfilled Fermi level, there exists the magnetic moment. However, even if n^* is known, the estimation of the moment also requires knowledge of the way in which these individual moments are coupled to create the collective moment of the surface state. We need something akin to Hund's rules for the spherical two-dimensional (2DEG).

Let us consider the case of *LS* coupling. By analogy with atomic physics for an NP with total momentum quantum number *J,* the magnetic moment can be written as

$$\mu_{l_F} = \mu_B g_J J\left(l_F, n*\right) \tag{12}$$

Where g_J is the Landé factor for the particular $2J + 1$ subspace corresponding to the quantum number J that is roughly proportional to the square of l_F.

In an assembly of nanoparticles, both r/a and α will present fluctuations with respect to their average values $\langle r/a \rangle$ and $\langle \alpha \rangle$ that will give rise, according to Eqn (11), to fluctuations in l_F and n^*. For a given value of l_F and a uniform distribution of n^*, the average value of the quantum magnetic moment is

$$\langle \mu \rangle_{l_F} = \mu_B \langle g_J J(l_F, n*) \rangle \tag{13}$$

$$\mu_{at} = \frac{3\langle \mu \rangle_{l_F} a^3}{4\pi r^3} \approx \langle g_J \rangle \mu_B \frac{\alpha\, a}{r} \tag{14}$$

$$m_d = -N_b \frac{e^2 B r^2}{4m} \tag{15}$$

The order of magnitude of the average $\langle \mu \rangle_{l_F}$ when n^* varies between 1 and $2(2l_F + 1)$ can be estimated, after approximating, $g_J = 1$ and $J = \frac{1}{3} l_F^2$, as

When a magnetic field is applied along the polar or z axis, as thoroughly analyzed in [120], the spectrum of the kinetic energy splits the degenerate ground state into its $2J + 1$ components and induces a diamagnetic moment, m_d, given by

The diamagnetic component is much larger than that usually observed for atoms as a consequence of the mesoscopic diameter of the orbits [121], but it remains almost negligible for $J \neq 0$ since, for $B = 1.0$ T, it is of the order of $10^{-3}\ \mu_B N_b$.

However, the paramagnetism is expected to overweigh the diamagnetism, since with surface collective magnetic moments of the order of $g\mu_B l_F^2$, for an applied magnetic field of 1 T would induce a maximum Zeeman splitting of $2\mu_B l_F^2$ that is larger than the thermal energy at room temperature for any

$l_F > 10$. It can be concluded that the Langevin or Brillouin curve describing the paramagnetism of the NPs is close to saturation, i.e. the condition $\mu_r l_F^2 B > 3k_B T$ holds for $B = 1.5$ T and T = 300 K when l_F is larger than 10.

5.6 Final Remarks

It has been generally accepted in the literature cited in this article that the origin of the ferromagnetic-like behavior observed in NPs formed by nonmagnetic substances is originated from point defects located at the surface of the NPs, and its contribution decreases as the size of the NP increases. Its strength can be modified by tuning the interactions of the surface atoms and the coating molecules. Although the intrinsic origin is not well understood, the use of selective techniques, such as Mossbauer and XMCD, has neatly indicated that the magnetism is intrinsic to the NP atoms. The main difficulty arises in accounting for the type of exchange interaction between the localized magnetic moments.

Different experimental results confirm that the modification induced in the electronic structure of the surface by the bonding to organic molecules is associated with modifications in the magnetic properties. It has been shown that two-dimensional confinement of electrons (or holes) introduced by capping molecules (or impurities) in previously empty surface states may be the source of the magnetic moments observed in Au nanoparticles. Similar to the intrinsic ferromagnetism of atoms promoted by the Hund rule in an unfilled orbital, there exists an intrinsic ferromagnetism at the surface of NPs with an unfilled Fermi level in their surface band.

6. CHEMICAL PROPERTIES

6.1 Introduction

In this section, some of the chemical properties of gold nanoparticles will be discussed with a special focus on the nature of the gold-sulfur surface; on the chemical properties of the monolayer surrounding MPCs and on the catalytic activity of supported and unsupported gold nanoparticles. Our understanding of the chemistry of the gold-sulfur interface experienced a tremendous development after the solid-state structure of small thiolate gold clusters became available, unveiling unprecedented structural motifs that challenged the long-standing model for alkanethiols adsorption onto gold surfaces. Earlier structural models consisting of the binding of thiolates at the vertices, edges, and facets of small, idealized nanocrystals, are now superseded. The ligand shell surrounding the particles is the region where the large majority of the chemical and physical events relevant to the interactions of MPCs with other molecular entities or more complex structures take place. The monolayer of these particles inherits the curvature of the core; as a consequence, there is enough room between different chains comprising the monolayer to embed

other small molecules. The monolayers are then expected to exhibit a host-guest chemistry on their own in addition to perhaps a more selective host guest chemistry imparted by a specific design of the monomers comprising the monolayer. The analysis of the structure of the monolayers containing mixtures of ligands with different properties put in evidence the existence of phase segregation phenomena with formation of domains of different sizes and shapes. This property of mixed monolayers was theoretically predicted and supported by thermodynamic arguments. The ability to govern the formation and morphology of these domains will become an essential tool for using the nanoparticles as building blocks in the preparation of self-assembled materials with predicted architecture and properties. Finally, the use of gold nanoparticles for catalytic purposes is nowadays not only a topic of mounting research interest, but also a technology that holds promise of practical applications in industrial processes. The number of reactions catalyzed by some form of heterogeneous gold nanoparticle catalyst is steadily increasing, with the gas-phase low temperature oxidation of CO remaining an archetypal process. However, gold nanoparticles protected by polymers or passivated by strongly chemisorbed ligands were also found to be catalytically active in either the supported or unsupported forms.

6.2 Surface Properties of Nanosize Gold

In discussing some details of the surface properties of nanosize gold particles, a first distinction has to be made with respect to the presence or absence of a passivating monolayer, AuNP or MPCs, respectively. Within MPCs, a second distinction must take into account the size of these materials because the present availability of structural information on atomically defined small metal clusters enables a rather precise description, while for larger passivated particles the surface properties may be inferred from our knowledge of smaller ones.

6.2.1 "Naked" Gold Nanoparticles

The reduction in the size of AuNPs leads to the onset of the size confinement effects described in other sections of this chapter; reduction in size also leads to a high surface to volume ratio, to an increase of surface atoms with reduced coordination, and to an increase of surface tension of the particle leading to bond contraction and, therefore, a contraction of the Au lattice parameters with respect to bulk gold [122], which was also detected in smaller Au clusters such as $[Au_{25}(SCH_2CH_2Ph)_{18}^{-}\ TOA^{+}]$. All these effects have a strong impact on the structure of the particles. The increase in surface energy, for instance, dictates their morphology but also their reactivity toward putative capping agents. The equilibrium morphology of gold nanoparticles in the size regime of 3−100 nm has been investigated by using first principle calculations and a thermodynamic model; according to the results, the predicted thermodynamic

equilibrium shape of monocrystalline AuNPs of this size is a truncated octahedron. This predicted stability with respect to other shapes is the result of the balance between the surface energies of the facets and the surface to volume ratio of the particle. A further development in analyzing the thermodynamic stability of this species and its temperature dependence based on relativistic *ab initio* calculations led to the construction of a quantitative phase map for gold nanoparticles, even for particles with sizes extending below the limit of 3 nm for which the predicted equilibrium morphologies are decahedra or icosahedra. This model at the temperature of 300 K predicts an icosahedra−decahedra transition at critical size of about 10 nm and a decahedra−truncated octahedral transition at the size of 14 nm. In general, the average coordination number of the gold atoms in a particle decreases abruptly below a threshold of about 300 atoms, corresponding to a nanoparticle size of about 2 nm. Regardless of the size, the most reactive sites were considered to be those with the smallest coordination found at the edges, vertices, and terraces of the particles. These atoms are held responsible for coordination of reagents in catalytic processes, being the binding energies of relevant species such as CO, dioxygen, and atomic oxygen, monotonic functions of the coordination number of the gold atoms in the clusters [123]. However, recently, the surfaces of AuNPs with truncated octahedral morphology, a size of about 3 nm, and having composition Au_N ($N = 923 \pm 23$) were proved to contain a large number of single adatoms [124], accounting for 70% of the total surface atoms by a study employing aberration-corrected scanning transmission electron microscopy (STEM) in the high-angle annular dark-field (HAADF) imaging mode. These adatoms are located at both the {100} and {111} facets with similar probabilities, and they were found to migrate dynamically from a facet to the others under simple thermal excitation. The presence of these adatoms at the AuNP surface, even in the absence of bound ligands, will have a significant impact in improving the understanding of the surface properties of these systems and their reactivity towards putative ligands or in catalytic applications.

6.2.2 Thiolate-Protected Small Clusters and Nanoparticles

Significant advances in our understanding of the nature and properties of the Au-sulfur interface came after the elucidation of the solid-state structure of small gold nanoclusters, with the determination of the structure of $Au_{102}(p\text{-MBA})_{44}$ and the subsequent theoretical investigations representing turning points [99,125]. The structural analysis of the $Au_{102}(p\text{-MBA})_{44}$ cluster revealed the Au atoms are in two different states, an ensemble of 79 atoms which can be described as metallic and packed in a Marks decahedron, while the remaining gold atoms, formally Au(I), are engaged in the formation of a protecting shell of composition $Au_{23}(p\text{-MBA})_{44}$ with the thiolates. The shell can also be considered as consisting of $RS(AuSR)_n$ units with $n = (1, 2)$, generally indicated as "staples." Monomeric staples if $n = 1$ (−RS−Au−SR−) or dimeric staples (−RS−Au−SR−Au−SR−) if $n = 2$ are bound to the Au_{79}

kernel by their terminal sulfur atoms [126]. Interestingly, the unit cell was found to contain an enatiomeric pair of clusters, the chirality arising from an equatorial band of 13 gold atoms bound to thiolate moieties with irregular positions. The overall symmetry of the cluster is C_2, the low symmetry resulting in the definition of a set of 22 symmetrically unique ligands. Shortly afterward, the determination of the structure of $[Au_{25}(SR)_{18}^{-}\ TOA^{+}]$ reinforced and corroborated the emerging staple structural model. In fact, this species may be considered as consisting of an Au_{13} core surrounded by the remaining 12 gold atoms and 18 thiolates arranged in six dimeric staples. These structural features were afterwards found to be entirely consistent with the superatom model that predicts high stability for those cluster compounds that feature a total electron count of 2, 8, 18, 34, 58, 92, 138, etc., for their inner kernel of electrons in a closed electron shell. The kernel of $Au_{102}(p\text{-MBA})_{44}$ and the kernel of $Au_{25}(SR)_{18}^{-}$ feature 58 and 8 electrons, respectively.

Presently, besides the structure of the aforementioned clusters, the structures of $Au_{38}(p\text{-}tBuC_6H_4S)_{24}$ [127], $Au_{38}(SCH_2CH_2Ph)_{24}$, $Au_{28}(p\text{-}tBuC6H4S)_{20}$, and $[Au_{23}(SC_6H_{11})_{16}^{-}\ TOA^{+}]$ are known, and the existence of staples seems to be a sort of common structural motif in all of these species, for $[Au_{23}(SC_6H_{11})_{16}^{-}\ TOA^{+}]$ trimeric staple motif was also identified. These findings are also in line with recent advances on the elucidation of the nature of the gold sulfur interface for 2D-SAMs, for which the established model of an unreconstructed Au(111) surface with adsorbed alkanethiols has been challenged by the increasing evidences for the presence of AuSR monomers and, at the early stage of alkanethiol adsorption, of RS−Au−SR motifs. The robustness of these binding motifs is supported by the known stability of the 2D-SAM of alkanethiols on Au(111), to which the gold−sulfur interaction contributes with about 208 kJ/mol and the van der Waals interaction between methylene groups contribute with an average of 6.24 kJ/mol. The structural model of small gold clusters consisting in a metal core surrounded by a shell comprising gold atoms and the thiolate moieties arranged in oligomeric structures of staple-like geometry has been used to rationalize the stability of much larger nanoparticles, at least for those for which a precise stoichiometry may be defined on the basis of structural or mass analysis. This is the case for the $Au_{333}(SR)_{79}$ molecule, and that was proposed to consist of an Au_{293} kernel surrounded by a shell of composition $Au_{40}(SR)_{79}$; although, an interpretation in terms of a combination of oligomeric staples remains undefined. Besides the existence of such unitary structural motifs, there is also some evidence for a strong influence of the nature of the ligands in dictating the precise nature of the gold-sulfur interface. In fact, while for the $Au_{38}(SCH_2CH_2Ph)_{24}$ clusters, it has been reported a structure consisting of a face-fused bi-icosahedral Au_{23} core, enclosed by a second shell comprising the remaining 15 gold atoms and the 24 thiolate moieties arranged in three monomeric and six dimeric staples, the related cluster $Au_{38}(p\text{-}tBuC_6H_4S)_{24}$ was found to be much less stable and to transform under relatively mild conditions into a novel $Au_{36}(p\text{-}tBuC_6H_4S)_{24}$

cluster. In this case, where direct conjugation of the aromatic ring with sulfur is possible, the influence of such conjugation seems to extend to the electronic properties of the whole cluster, including the geometry of the inner kernel, and not only restricted to the passivating shell [127]. All of these findings suggest that the understanding of the "staples" chemistry and, in a more general way, the understanding of the interface chemistry of thiolate-protected clusters will probably be a future field of intense investigation because it is now recognized that the gold−thiolate oligomeric interfacial structures have a strong influence on the physicochemical properties of small thiolate-protected gold clusters, such as photoluminescence and chiroptical activity. An example of the rich diversity that may be encountered can be found in the recently reported solid-state structure of Au−Ag intermetallic clusters of general formula $Au_{12}Ag_{32}(SR)_{30}$ protected by different fluorinated arylthiols [128]. In this case, an otherwise unstable Au_{12} icosahedral kernel is encapsulated by an Ag_{20} cage surrounded by a metal−ligand shell consisting of six three-dimensional $Ag_2(SR)_5$ units in which Ag cations bind to three thiolate ligands in a planar $Ag(SR)_3$ configuration.

6.2.3 Reactivity at the Gold−Sulfur Interface

One of the most important chemical properties of the gold−sulfur interface of alkanethiolate-protected gold nanoparticles is the possibility to sustain exchange reactions replacing a ligand with another without affecting the structural integrity of the particles. In fact, the large majority of reports on the preparation of particles featuring mixed monolayers exploit this synthetic route. A number of evidences collected during the past years indicate that the process is associative and occurs in a 1:1 stoichiometric ratio, somehow resembling a direct displacement reaction of S_N2 character. A more detailed picture of this reaction comes after the structural elucidation of a partial exchange product on the $Au_{102}(pMBA)_{44}$ cluster [129], and by subsequent theoretical analyses of the process. The structure of the cluster $Au_{102}(pMBA)_{40}(pBBT)_4$, obtained by reacting the well-characterized cluster $Au_{102}(pMBA)_{44}$ with *p*-Bromo benzenethiol (pBBT) under kinetic control, revealed that two of the 22 symmetry unique positions on the cluster shell were quickly exchanged, with these two positions being solvent accessible, hence exposing Au atoms also accessible to the incoming ligands. The mechanism of this exchange was studied by DFT methods on a model system replacing the bound thiolates with −SH residues and the incoming ligand with methanethiol. This special reactivity at certain sites of the monolayer of small gold clusters parallels the reactivity of larger particles that were found to be amenable of functionalization at their polar position. In this case, the special reactivity was the result of a well-defined morphology of the monolayer [130]. With reference to Figure 10, the preferred pathway was found to require the development of a bond between the sulfur atom of the incoming ligand the central gold atom engaged in the

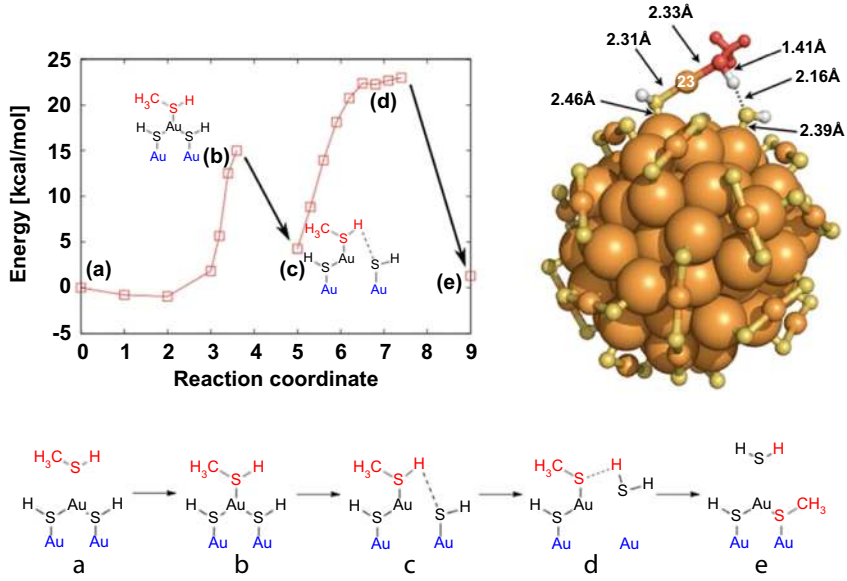

FIGURE 10 Proposed mechanism for the place exchange reaction on a $Au_{102}(SH)_{44}$ gold cluster by an incoming methanethiol as a model for the place exchange reaction of the $Au_{102}(p\text{MBA})_{44}$ with *p*-bromo benzenethiol. *From Ref. [129].*

formation of a staple (b). This event is followed by a step (c) in which an intermediate is formed by dissociation of the bond connecting the gold atom to the terminal thiolate in the staple, the latter being stabilized by the formation of a hydrogen bond with the hydrogen of the incoming thiol. This hydrogen bond evolves into a full proton transfer (d) releasing the thiolate originally involved in the formation of the staple into solution as a thiol (e), leaving a kernel gold atom that connects to the sulfur of the incoming thiol, restoring the initial geometry of the system. The net balance is, therefore, the substitution of one thiolate unit with the release of a thiol into solution, the process involving the Au central center involved in the staple.

This mechanism, however, is probably a simplification and further studies are needed to understand the reactivity of nonexposed Au atoms toward the exchange reaction. Another long standing issue that will require a deeper understanding of the "staple chemistry" is the lateral mobility of the thiolates within the ligand shell. At present, evidences of such a mobility in small alkanethiolate-protected gold clusters exist [131], but the precise mechanism is unknown, being, in principle, the net result of a dissociative−associative process with the release of thiolates into solution or an "on surface" migration of the thiolates.

The presence of staples motifs on the surface of the gold core has another remarkable effect: the formation of intrinsically chiral gold clusters that do not present in their ligand shell chiral thiolates.

The chirality arises from the substitution pattern at the sulfur centers in the staple units; in fact, the sulfur atoms have three different substituents: the surface Au atom, the R residue, and the gold atom involved in the staple motif. Therefore, the sulfur is a stereocenter as it is, for instance, in trisubstituted sulfonium ions. This kind of intrinsic chirality, first identified for the $Au_{102}(p\text{-MBA})_{44}$ cluster was also found for $Au_{38}(SCH_2CH_2Ph)_{24}$ [132]. Clearly, these compounds are formed as racemic mixtures, and in the solid state, the unit cell contains two molecules of opposite handedness. In these two cases, the chiral nature of the clusters was put in evidence from the elucidation of their solid state structure by X-ray analysis. For $Au_{38}(SCH_2CH_2Ph)_{24}$, the two enantiomers were successfully separated by chromatographic methods and the enantiomeric nature of the species isolated was established by recording their CD spectra that are mirror images of one another [133]. The two enantiomers are sufficiently stable but the energy barrier for their interconversion is low, about 116 kJ/mol, leading to significant racemization at 40 °C. The compound $Au_{40}(SCH_2CH_2Ph)_{24}$, was also found to be racemic, and the two enantiomes were separated by using chiral chromatography. The intrinsic chirality of some gold clusters also has an implication on the reactivity of these clusters with chiral thiolates in the place exchange reaction. Indeed the exchange reaction of the racemic $Au_{38}(SCH_2CH_2Ph)_{24}$ cluster with *R*-1,1′-binaphthyl-2,2′-tithiol (*R*-BINAS) to give the mono- and disubstituted products $Au_{38}(SCH_2CH_2Ph)_{24\text{-}2x}(R\text{-BINAS})_x$ ($x = 1,2$) was found to be diastereoselective [134]. Another way to impart chirality to a gold cluster is to introduce chiral thiolates in their ligand shell; this often results in the induction of a cotton effect on the electronic transition of the gold core. Such behavior has been reported for the Au_{25} clusters protected by 2-phenyl-propane-1-thiol [135] or the enantiopure 1*S*, 4*R*-camphorthiol [136].

6.3 Catalytic Activity

With reference to heterogeneous catalysis, several factors contribute to the definition of the catalytic activity of these systems, primarily the nanoparticle size and the chemical nature of the support. With respect to the first aspect, nanostructures with size in the range of 0.5−5 nm seem to be preferred. An emerging strategy allows the achievement of precise control over the AuNP size consists in supporting preformed thiolate passivated nanoparticles with controlled size and composition; in this case, the protecting monolayer may be retained or removed depending on the thermal processing of the catalyst prior to use. The role of the substrate is of primary importance in modulating the properties of the supported particles, and the existence of a strong metal−support interaction (SMSI) with charge transfer between the support and the AuNP has been recognized in several cases. The substrate also provides active sites for the activation of the species involved in the reaction. In this respect,

reducible metal oxides such as TiO_2, CeO_2, Fe_2O_3, and Fe_3O_4 seem to be the best substrates in addition to ZrO_2, ZnO, SiO_2, and Al_2O_3. However, other supports such as zeolites and carbonaceous materials have been successfully employed. In addition, the support provides a medium to anchor the particles, thus limiting their thermal sintering under high temperature conditions that are sometimes encountered during practical operation or catalysts pretreatment, generally resulting in catalysts deactivation. A strategy deployed to mitigate the occurrence of sintering processes exploits the preparation of encapsulated gold nanoparticles [137] or the supporting of metal nanoparticles inside the pore channels of mesoporous materials, such as mesoporous SiO_2 and TiO_2 [138]. In these cases, encapsulation also provides a mechanism of selectivity tuning of reagents and products. Alternatively, MPCs may also be used to engineer materials, as in the case of Au@CeO_2 formed by the precipitation method using MPCs comprising in their ligand shell water-soluble polyether thiolates and alkanethiolates terminating with a carboxylic group to interact with the CeO_2 precursors. After calcination, these materials were found to be active catalysts in the oxidation of CO under PROX conditions [139]. Despite the wealth of reports on AuNP catalysis, the precise nature of the catalytic sites on both the AuNPs and the support is very often unclear and is a subject of debate; either small metallic clusters of Au(0), partly oxidized ($Au^{\delta+}$), or reduced particles ($Au^{\delta-}$) formed by interaction with the substrate or in the preparation of the catalyst in addition to undercoordinated gold atoms or Au(I) and Au(III) may act as the actual active sites [140,141].

6.3.1 Catalysis in Oxidative Processes

Perhaps the most studied oxidation reaction catalyzed by supported AuNPs is the gas phase aerobic oxidation of CO, the best catalysts being Au/CeO_2 and Au/TiO_2. As mentioned above, for a given substrate, the size of the AuNPs is crucial in determining the efficiency of the catalysts, with an optimal size range of 0.5−5 nm being preferred. Concerning the low temperature CO oxidation and the somewhat related WGSR, the AuNP/CeO_2 contact interface is considered the catalytically active region [142], as could be inferred from the proportionality between the rate of CO oxidation and the length of the perimeter interface [143]. The CO adsorption sites are located on the gold particles and, in the case of AuNPs supported on nanocrystalline CeO_2, the presence of Au^{3+}, Au^{+}, and Au(0) species has been demonstrated by IR exploiting the characteristic Au−CO frequencies [144]. The reactivity of this catalyst was also correlated to the concentration of cationic Au^{3+}, but not with the concentration of Au^{+} or Au^{0} species. The ceria support is primarily involved in stabilizing dioxygen. The form of the adsorbed dioxygen being related to the precise nature of the ceria support, while nanocrystalline ceria stabilizes dioxygen as peroxide and superoxide species, precipitated ceria stabilizes dioxygen as O_{2d}^{-} or molecular O_2. Thus, simplifying, the gold particle adsorbs CO, while the ceria support activates molecular oxygen through

the participation of its lattice oxygen. More recently [145], in the CO oxidation using Au/CeO_2 nanorods, a mechanistic study that included the use of isotopicaly labeled dioxygen confirmed that upon exposure of CO to the catalyst, CO_2 was immediately formed, supporting the idea that the support supplies the reactive oxygen species for the oxidation. After a pulse of $^{18}O_2$ to restore the stoichiometry of the ceria support and the subsequent introduction of CO, the production of $C^{16}O^{18}O$ was detected by mass analysis. Although in this case, the possible role of cationic Au was not explored; this picture is consistent with previous findings [144] and recent DTF calculations [146] which additionally provided substantial structural insight for the cationic nature of the species involved in the oxidation of CO. Interestingly, the typical catalysts for CO oxidation such as Au/CeO_2 and Au/TiO_2 seem to undergo morphological changes under the reaction conditions, as was recently reported by environmental transmission electron microscopy (ETEM) [147]. These findings will probably add new information in elucidating the mechanism of these processes. However, the precise mechanism of CO oxidation may be dramatically different when different supports are considered. It is now well established, for instance, that the presence of moisture in the gas stream is beneficial in increasing the catalyst efficiency [148], although the magnitude of this effect depends on the nature of the substrate and seems to be remarkable for relatively poor catalysts such as Au/SiO_2 or Au/Al_2O_3. This observation, in addition to the ability of water to regenerate inactivated catalysts, points in the direction of a direct involvement of hydroxyl groups in the catalytic cycle, at least in the case of substrates such as TiO_2 [149] and Al_2O_3 [148]. In the former case, oxygen exchange was observed between adsorbed atomic oxygen and isotopicaly labeled water. Coadsorbed water ($H_2^{18}O$) takes part in CO oxidation on oxygen adatoms precovered $Au/TiO_2(110)$ model catalysts, leading to the formation of $C^{16}O^{18}O$ and $C^{16}O^{16}O$. For catalysts such as Au/Al_2O_3, a kinetic model comprising the formation of adsorbed hydroxyl and hydroperoxy (OOH) species was proposed, with the hydroperoxy species reacting with CO producing CO_2 and OH, since in this case, exchange between $^{18}O_2$ and $^{16}O_2$ and between $H_2^{18}O$ and $H_2^{16}O$ was not observed, while the dissociation of dioxygen was excluded as a mechanistic relevant pathway in the Au/Al_2O_3 catalyzed reaction [150]. The involvement of hydroxyl species is also considered to be relevant in the CO oxidation processes carried out in aqueous solutions [148].

As mentioned, the catalytic activity of metal nanoparticles is size dependent, with small particles being the most active. Therefore, a precise control of the particle size represents a possible strategy in improving the performance of a supported catalyst. In this respect, the methodologies developed for the synthesis of MPCs may be considered a useful tool. Indeed, materials obtained by supporting small thiolate-protected clusters were found to be active in CO oxidation; for instance, the cluster compound of well-defined composition $Au_{25}(SCH_2CH_2Ph)_{18}$ supported, by impregnation, on CeO_2 proved to be active

in the CO oxidation with the onset of catalytic activity at 60 °C; whereas, a similar TiO_2 supported catalyst was found to be much less active [151]. Also in this case, the interface between the gold cluster and the support was reported to represent the catalytically active region in analogy with other supported Au/CeO_2 catalysts. The same cluster, in addition to $Au_{38}(SCH_2CH_2Ph)_{24}$, and $Au_{144}(SCH_2CH_2Ph)_{60}$ supported onto SiO_2 and hydroxyapatite without calcination treatment, thus retaining their ligand shell, displayed to be active in the oxidation of styrene by dioxygen in the presence or absence of TBHP as initiator or by TBHP as the oxidant, selectivity being toward benzaldehyde [152]. For this reaction, a tentative mechanism requiring coordination of both dioxygen and styrene on the surface of the gold clusters was proposed. Similarly, glutathione (GSH)-protected clusters of composition $Au_{10}(SG)_{10}$, $Au_{18}(SG)_{14}$, $Au_{25}(SG)_{18}$, and $Au_{39}(SG)_{24}$ supported on hydroxyapatite were found to be active in the oxidation of cyclohexane to cyclohexanol and cyclohexanone, although with limited selectivity [153].

6.3.2 Catalysis in Hydrogenation Reactions

Supported gold particles are active catalysts in the reduction of a variety of organic compounds; the majority of the studies are related to solution phase reactions carried out at high temperature and high hydrogen pressure. The reactivity in these cases is due to the heterolytic dissociation of hydrogen on the surface of nanosize gold. The heterolytic pathway requires that the formal H^- resides on gold, while the formal H^+ protonates the support as was demonstrated by inelastic neutron scattering and IR spectroscopy investigations [154,155]. The stability of the resulting Au—H is rather low when compared to the hydrides of Pd and Pt, and consequently, the concentration of Au—H entities is low. This results in a remarkable selectivity of the AuNP-catalyzed hydrogenation reactions. Typical supports for AuNP-mediated hydrogenations are SiO_2, Al_2O_3, ZrO_2, ZnO, CeO_2, and TiO_2. The spectrum of catalyzed reactions is rather wide and comprises hydrogenations of unsaturated C—C bonds, hydrogenation of carbonyl compounds, and CO_2 and hydrogenation of nitro compounds. The reactions are remarkably selective. For instance, the reduction of an aldehyde group in an α,β-unsaturated compound can be carried out safely in the presence of double bonds, and the reduction of the nitro group can be carried out in the presence of aldehyde moieties. From the mechanistic point of view, these reactions are difficult to study because of the conditions employed, and the picture is often complicated by the reactivity of ionic gold species or complexes that are themselves active catalysts under homogeneous conditions.

6.3.3 Catalysis by Unsupported Gold Nanoparticles

Although the support plays a fundamental role in dictating the reactivity of AuNPs, these species may act as catalysts even in the absence of support in reactions similar to those catalyzed by supported AuNPs. In this respect, the

large majority of the cases relate to polymer-stabilized nanoparticles such as polyvinylpyrrolidone (PVP) and polyvinyl alcohol (PVA) in addition to polyamidoamine dendrimer (PAMAM)-stabilized AuNPs [156–158]. Among these catalysts, MPCs and "naked" or citrate-stabilized AuNPs are also included. Several reactions are catalyzed by these systems, comprising alcohol oxidations, epoxydations, CO oxidation, hydrogenations, and the oxidation at the benzylic position of aromatic hydrocarbons. Decreasing the size of the nanoparticles, higher catalytic activities are obtained, as it was observed for supported AuNPs. Instead, increasing the steric hindrance due to the presence of stabilizing molecules on the gold surface reduces the catalytic efficiency of the systems, even if the nanoparticle size is unchanged. Most notably, the small, thiolate-protected clusters $Au_{25}(SCH_2CH_2Ph)_{18}$ are active catalysts in the hydrogenation of benzalacetone [159] with hydrogen at atmospheric pressure, and in the reduction of *p*-nitrophenol [160]. The same system was also active in the chemoselective hydrogenation of benzalacetone without affecting the C–C double bond [161]. Other small thiolate-protected clusters such as $Au_{38}(SCH_2CH_2Ph)_{24}$ and $Au_{144}(SCH_2CH_2Ph)_{60}$ were also active in the solution phase oxidation of styrene to benzaldehyde, styrene oxide, and acetophenone, with selectivity towards benzaldehyde. When these particles retain their ligand shell during the catalytic process, a novel source of selectivity becomes available: the interaction of the reactants within well-defined "binding pockets" on the surface of the nanoclusters, as was found in the case of the stereoselective reduction of a bicyclic ketone in the presence of the $Au_{25}(SCH_2CH_2Ph)_{18}$ cluster [162].

6.4 Characteristics and Properties of Monolayers Grafted on the Gold Surface

The monolayer surrounding the nanoparticles represents the interface connecting the nanoparticles with the external environment. Looking at nanoparticles as "interfacial materials," it is in a region close to the outer surface of this monolayer that the large majority of the chemical and physical events relevant to the interactions of MPCs with other molecular entities or more complex structures take place. The monolayer of these particles inherits the curvature of the core. As a consequence, there is enough room between the different chains comprising the monolayer to embed other small molecules. The monolayers are then expected to exhibit a host–guest chemistry on their own, in addition to perhaps a more selective host–guest chemistry imparted by a specific design of the monomers comprising the monolayer. A relevant question arises when the monolayer comprises a mixture of thiolates: a mixed monolayer has to be considered as consisting of random distribution of thiolates or should phase segregation be expected in analogy with other self-assembled systems? The answer was in the positive; indeed, phase segregation with formation of domains of different sizes and shapes was

experimentally evidenced, and this finding was theoretically predicted and supported by thermodynamic arguments. The evidences of domains with different properties on the surface of nanoparticles and the ability to master their preparation will become an essential tool in using the nanoparticles as building blocks for the preparation of self-assembled materials with predicted architecture and properties.

6.4.1 Monolayer Morphologies, Experiments, and Theoretical Investigations

When a mixture of thiols is assembled on the surface of gold nanoparticles, mixed monolayer gold nanoparticles (MMPCs) arise. The first direct information on the organization and microscopic structure of mixed monolayers on the surface of nanoparticles was obtained by STM in the group of Stellacci, revealing a high degree of order with the formation of well-defined stripe-like domains of unlike thiols. Further studies revealed that the formation of striped domains is favored in particles with sizes within a well-defined size regime between about 2.5 and 8.0 nm [163]. Improvements in the STM analyses allowed the achievement of quasimolecular resolution in imaging these structural features of mixed monolayer nanoparticles [164]. In particular, it was possible to highlight the presence of aligned features with a spacing of 1 nm between consecutive lines. In the same analysis, the presence of the headgroups of the thiolates within the stripes could be clearly evidenced with a spacing of about 0.5 nm. The interpretation of STM images is often cumbersome, but recently by analysis of the topographical power spectral density (PSD) of the STM data, the characteristic length scales of the features exhibited by nanoparticles in STM images could be obtained in a straightforward manner [165]. Another analytic method that proved to be valuable in addressing the structure of MMPCs is the matrix-assisted laser desorption/ionization ion mobility mass spectrometry (MALDI-IM-MS) [166]. The reason for the sensitivity of this technique in probing the monolayer structure is that the main species formed upon laser desorption/ionization, the Au_4L_4 ions, deriving either from desorption from the gold surface or from the rearrangement of staple motifs, are recognized to reflect the local composition of the monolayer. The relative abundance of fragments with a given composition is, therefore, correlated to the structure of the original monolayer. The assessment of the monolayer morphology is obtained by comparing the experimental data to theoretical abundance patterns derived from an idealized model of the monolayer, constructed assuming a specific morphology. This approach was found to be particularly useful to highlight a rather surprising feature, that is: the MMPCs obtained by direct synthesis exploiting a mixture of two thiols seem to display little phase segregation, while nanoparticles obtained by the place exchange reaction seem to display more pronounced phase segregation.

Another technique used to gain information on the structure of the monolayers is nuclear magnetic resonances, by exploiting (1) the sensitivity of the chemical shifts of the molecules in the monolayer to their chemical environment and (2) the Nuclear Overhauser Effect established between chains sufficiently close in space, Figure 11. In a random distribution of thiolates, the local and global composition of a monolayer are similar; this similarity breaks down when the monolayer presents a defined morphology. Since the chemical shift depends on the environment experienced by the probe nuclei, differences in local and global compositions and, hence, phase segregation could be evidenced by this method [167]. Notably, for nanoparticles featuring stripe-like domains, a sigmoidal dependence of the chemical shift with respect to the composition is expected (Figure 11(C)). Whereas, for Janus particles, with two well-separated macro domains, a hyperbolic dependence should arise (Figure 11(B)). If no phase segregation is present, the relationship between the chemical shift and the composition should be linear (Figure 11(A)). In the presence of monolayers with randomly distributed thiolates or with stripe-like domains, significant cross-peaks in the

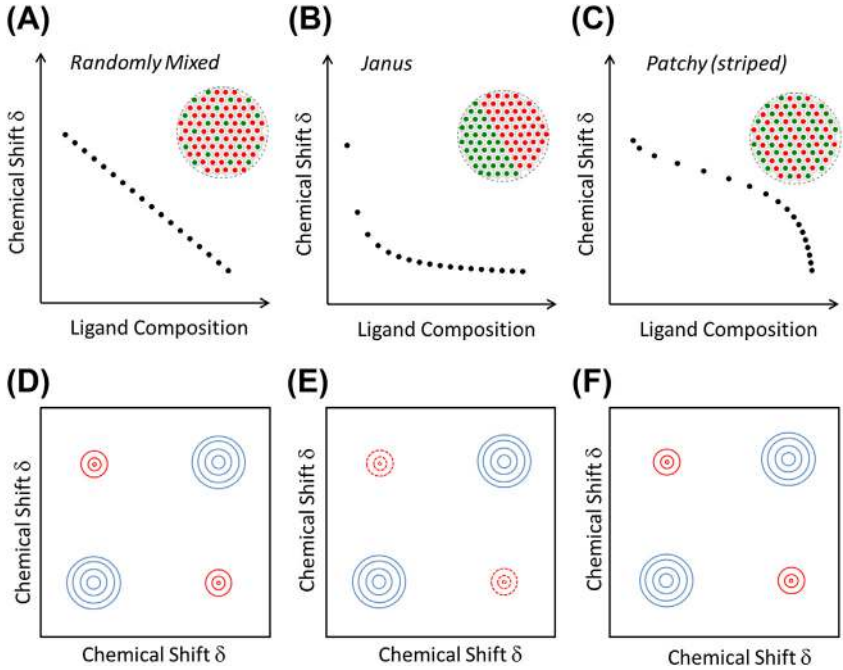

FIGURE 11 Predicted NMR patterns for nanoparticles coated with a binary mixture of ligands. Panels A, B, and C represent the expected chemical shift dependency upon monolayer composition for randomly mixed (A), Janus (B), and striped (C) nanoparticles. Panels D, E, and F represent the NOESY pattern expected for randomly mixed (A), Janus (B), and striped (C) nanoparticles. *Figure adapted from Ref. [167].*

NOESY spectra of the particles should be visible (Figure 11(F)). On the contrary, cross-peaks should be negligible if complete separation of the thiolates in two macrodomains occurs as in Janus particles (Figure 11(E)). This two experiment set enables us to characterize the monolayer morphology of MMPCs with an easily accessible technique. Indeed, nanoparticles with a core diameter of 5 nm and containing diphenylthiol and dodecanthiol with different compositions were shown by this method to present stripe-like domains in their monolayer. Smaller particles displayed the behavior expected for Janus particles. Instead, nanoparticles featuring a disordered monolayer comprising 3,7-dimethyloctanthiol and diphenylthiol displayed a linear dependency of the chemical shift toward the composition. The experimental findings on the occurrence of domains on the monolayer of nanoparticles were the subject of intense theoretical analysis, and the results fully support the experimental data. The group of Glotzer contributed to this field with a thorough investigation of the factors triggering the spontaneous formation of domains [168]. From a qualitative standpoint, it is reasonable that unlike ligands will tend to self-sort into different domains, thus minimizing their reciprocal interactions as it is observed in the case of other self-assembled systems. This phase segregation observed in MMPCs results from the interplay between thermodynamic and geometric factors, stemming from the chemical "dissimilarity" of the ligands forming the monolayer and the size of the nanoparticle core. The former comprises "true" chemical dissimilarities or a geometrical mismatch due to, for instance, differences in length of the thiolate chains. The latter is mainly related to the conformational freedom and, hence, conformational entropy of the thiolate chains located at the boundaries of different domains, which also function on the monolayer curvature. Hence, in this framework, specific morphological arrangements that allow a certain degree of conformational entropy to be achieved would be favored. In a tightly packed monolayer comprising long and short thiolates, the one that can be obtained by self-assembly on a large particle with small curvature, a reasonable gain in conformational entropy may be obtained only for those thiols located at the boundaries of the domain separating long and short ligands, with the long benefitting from an increase in conformational entropy due to the free room available for bending over the short ligands. It is, therefore, reasonable to conclude that in the case of ligands with significant differences in length, the minimization of the free energy of the system will require the maximization of the number, or the total length, of these boundary regions. For particles of size in the 2.5−8.0 nm regime, the formation of stripe-like domains is favored. However, for larger nanoparticles, the formation of worm-like domains without specific orientation is favored. For smaller particles, instead, for which a certain degree of conformational entropy is already ensured due to the free room available to the ligands because of the curvature of the particle, this picture is significantly changed, with the enthalpic term playing a major role, and the formation of Janus particles with

well-separated macrodomains being favored. Hence, when a binary mixture of "dissimilar" thiolates is adsorbed on the surface of a metal nanoparticle, both experimental and theoretical evidences exist that essentially three main morphologies may arise: (1) the formation of the so-called Janus particles, with complete segregation of the different ligands on the two halves of an idealized spherical surface, (2) the formation of striated domains orthogonal to one of the axes of the idealized sphere, usually referred to as "stripes," and (3) the formation of worm-like striated domains with no orientation with respect to the symmetry elements of the sphere. This picture is the result of considering binary mixtures of thiols, when a ternary mixture or quaternary mixture of thiols is considered; a rich variety of morphologies is possible as recently highlighted by theoretical investigations by Glotzer [169]. If a ternary mixture of thiols is considered, the simplest monolayer morphology for small particles predicted is the "Cerberus" nanoparticle, with three domains displaying an interface region with one domain and another interface region with the other domain. These are the ternary equivalent of the Janus particles. For quaternary mixtures, tetrahedral particles with the four ligands that generate four domains that minimize the interface between all ligand pairs are formed, with all the longest ligands forming an interface with the shortest. This arrangement is found for small particles compared to the ligand length. If the set of ligands comprises two long and two short ligands, the predicted geometry is that of a "Brahma" particle, with four domains arranged in such a way that the two longest ligands do not share an interface. By increasing the particle size and increasing the interaction strength between the ligands, a rich variety of morphologies results. If the composition of the mixture is largely unbalanced, with one of the thiolates representing the large majority of the mixture, the formation of isolated domains or patches is possible. Patchy particles with multiple patches arranged in a well-defined geometric pattern are presently actively studied from the theoretical point of view as anisotropic building blocks to construct superstructures via the interaction of patches located on different particles [170]. This strategy, once the synthetic control over the formation of patches is achieved, would probably represent an important tool for the future development of material science.

6.4.2 Properties of Mixed Monolayers that Feature Monolayer Domains

Nanoparticles coated with striped domains have many unique structure-dependent properties that mainly derive from their interfacial interactions. MMPCs coated with binary mixtures of octanethiol and mercaptopropionic acid of different compositions display solubilities with a marked non-monotonic behavior with respect to the monolayer composition. The solubility, therefore, depends critically on the surface morphology; the same applies to the surface-wetting behavior of these systems [171]. An unprecedented property of these nanoparticles is their ability to trespass the plasma membrane

of cells. Translocation across the membrane occurs by an energy-independent mechanism with no evidence of membrane poration or cell death. On the contrary, nanoparticles with the same composition but with random distributions of the thiolates on the monolayer were mostly trapped in endosomes [172]. A mechanism put forth in order to explain the observed effects relies on a two-step process which first requires the fusion of the nanoparticles with the membrane to form a transmembrane configuration, which eventually evolves toward a translocation into the cytosol. As a first step to validate this mechanism, a simplified model exploiting MMPCs contained in the monolayer 11-mercaptoundecane sulfonate (MUS) and octanethiol (OT) was tested with model lipid bilayers [173], both experimentally and theoretically. The theoretical analysis showed that nanoparticle composition and diameter, rather than morphology, were the most critical parameters in determining the free energy of interaction, the driving force being the reduction of the hydrophobic surface exposed to the solvent upon fusion with the membrane. The nanoparticle−membrane fusion is also accompanied by a significant distortion of the monolayer, forcing the charged groups out of the bilayer.

Nanoparticles with a mixed monolayer comprising 3-mercapto-1-propanesulfonic acid (MPSA) and different alkanethiols and featuring stripe-like domains were also showed to act as a catalyst in the acetylation of benzyl alcohol with acetic acid. A structure−reactivity analysis evidenced that the highest reactivity could be obtained for particles with an MPSA:octanethiol ratio of 2:1, confirming a role of the morphology on the reactivity [174]. Nanoparticles featuring stripe-like domains made of hexanethiol and polyethylene-glycol-terminated thiolates were shown to be active materials in the construction of a sensor for the determination of metal ions in solution with an unprecedented attomolar limit for the detection of methylmercury [175].

An extreme example of ligand dissimilarity driving the formation of domains on mixed monolayers is the one obtained by exploiting the known immiscibility of fluorous and hydrocarbon phases. When mixtures of PEGylated ligands that feature hydrocarbon chains and fluorocarbon chains are coassembled on the surface of gold nanoparticles, complete phase segregation takes place, even at very low loading of the fluorinated compound, as was recently inferred from ESR studies of the binding of a radical probe to the monolayer of mixed monolayer nanoparticles and by mesoscale simulations [176]. In this case, the formation of domains occurs even at loadings of the fluorinated thiolate as low as 4%.

6.4.3 Complexing Properties of Monolayers on Gold Nanoparticles

Another important feature of the monolayer surrounding the particles is its ability to complex molecules from a solution phase, thus forming a “loaded” nanoparticle. Several reports indicate that indeed monolayers have a significant ability to complex molecules, either by unspecific interaction or because

of a judicious selection of the nature of the monomers. The unspecific interactions result in hydrophobic binding of hydrophobic guests to the inner regions of the monolayer. While in general, the tailored binding is due to the interaction of target molecules with specific recognition moieties on the outer surface of the monolayer; in this respect, nanoparticles may be considered exo-receptors. The outer surface of monolayers was exploited as the place for a further self-assembly, as it was demonstrated by the assembly of catalytic peptides onto the surface of cationic gold nanoparticles featuring trimethylammonium groups on their surface. The catalytic performance of the system was also enhanced by the complexing ability of the monolayer toward the substrate of choice [177]. A similar approach exploiting nanoparticles coated with a homoligand monolayer of thiolates that bear as a terminal group a triazacyclononane moiety complexed with Zn(II) [178] allowed the development of a system amenable to the interaction of oligophosphonates and oligocarboxylates in water, with binding constants in the μM region. Other such exo-receptors that exploit electrostatic interactions between ionic groups located on the surface of the nanoparticles and charge complementary guests have been developed for the interactions with proteins and for the transfection of nucleic acids.

The complexing ability of the monolayer of nanoparticles is, however, not restricted to binding events on the outer surface. Hydrophobic binding may occur at the inner region of the monolayer, as could be evidenced by early studies exploiting ESR and a hydrophobic radical probe [179]. This technique also allows the identification of the region of the monolayer involved in the binding events because of the sensitivity of the ESR spectral parameters of the probe as a function of the polarity of the environment. Extending this approach to nanoparticles featuring a mixed monolayer of hydrogenated and fluorinated thiolates bearing terminal polyether moieties allowed to highlight that the binding preferentially takes place in the fluorinated domains of the monolayer [176]. The overall binding constant depended on the composition of the monolayer and was found to be in the range of 100−180 M^{-1}; the calculation of the binding constant for the fluorinated and hydrogenated domains confirmed a preferential binding to the former, with binding constants in the range 200−762 M^{-1}. Interestingly, the binding constants increase with decreasing content of fluorinated thiolates. Mesoscale simulations aided the rationalization of this behavior by displaying that at low loading of the fluorinated thiolate, its polyether chain has sufficient conformational freedom to bend over the shorter hydrogenated ligands, allowing a better recognition of the probe molecule. The apparent overall binding constants reported for the complexation of this probe are in the same order of magnitude of those reported for the complexation of the salicylate anion [180] by using homoligand monolayer nanoparticles prepared with polyetherterminated amphiphilic thiolates. The binding constant reported was 120 ± 5/M. This study employed NOE pumping experiments

that allowed the transfer of magnetization from the particle to the complexed species. Comparison of the binding constants of other anionic species allowed the conclusion that the binding was exquisitely related to the hydrophobicity of the probes. However, by introducing a zwitterionic thiolate derived from phosphorylcholine and extending the length of the hydrocarbon chain of the amphiphilic thiolate, the selectivity changed, indicating that both the size of the hydrophobic region in the coating monolayer and the specific interactions with the thiol endgroup affect the binding affinity. Another example of hydrophobic binding is the achievement of nanoparticle-based systems that are capable of transporting small molecule drugs into cancer cells [181]. These few examples serve to illustrate the potential of the monolayer surface to act as a scaffold for the assembly complex supramolecular even in the very competitive solvent water, and the potential of hydrophobic binding for the development of nanoparticle-based carrier systems.

7. CONCLUDING REMARKS

The development of novel nanoparticle-based technologies is strongly dependent on the advances in our understanding of their basic physical and chemical properties. Examples of this interconnection can be found in the ultrasensitive detection of analytes by Raman spectroscopy, achieved by exploiting the surface properties of gold nanoparticles. Other properties, such as the peculiar electron transfer dynamics of gold nanoparticles and other nanoscale entities, are of critical importance for the fabrication of next-generation electronic circuitries and devices, and the self-sorting of thiolates on MMPCs holds promise to become a tool for the bottom-up engineering of novel materials. Other examples are presented in details in this volume. The unprecedented properties of nanosize matter will likely continue to surprise and demand for better experimental and theoretical investigations and models. The understanding of the basic physical and chemical properties of gold nanoparticles is, therefore, not only important per se, but allows the development of new experimental techniques providing fundamental knowledge for the implementation of novel technological platforms.

ACKNOWLEDGMENTS

Patricia Crespo, Miguel Angel García and Antonio Hernando wish to acknowledge funding from the Spanish Ministry of Science and Innovation under project MAT2012-37109-C02-01.

Paolo Pengo and Lucia Pasquato wish to acknowledge funding from the University of Trieste (FRA 2011, 2012, 2013) and the Italian Ministry of Health, under project GR-2009-15779849.

REFERENCES

[1] K.C. Grabar, R. Griffith Freeman, M.B. Holmmer, M.J. Natan, Anal. Chem. 67 (1995) 735–743.
[2] S.A. Maier, Plasmonics: Fundamentals and Applications, Springer, 2007.
[3] U. Kreibig, M. Vollmer, Optical Properties of Metal Clusters, Springer, Berlin, 1995.
[4] V. Amendola, M. Meneghetti, J. Phys. Chem. C 113 (2009) 4277–4285.
[5] K.L. Kelly, E. Coronado, L.L. Zhao, G.C. Schatz, J. Phys. Chem. B 107 (2003) 668–677.
[6] Y. Xia, N.J. Halas, MRS Bull. 30 (2005) 338–348.
[7] P.K. Jain, M.A. El-Sayed, Nano Lett. 7 (2007) 2854–2858.
[8] V. Amendola, Synthesis of Gold and Silver Nanoparticles for Photonic Applications, Università degli Studi di Padova, Padova, 2008.
[9] K. Lee, M.A. El-Sayed, J. Phys. Chem. B 110 (2006) 19220–19225.
[10] V.M. Shalaev, S. Kawata, Nanophotonics with Surface Plasmons, Elsevier, 2006.
[11] C.A. Mirkin, R.L. Letsinger, R.C. Mucic, J.J. Storhoff, Nature 382 (1996) 607.
[12] E. Messina, E. Cavallaro, A. Cacciola, M.A. Iati, P.G. Gucciardi, F. Borghese, P. Denti, R. Saija, G. Compagnini, M. Meneghetti, V. Amendola, O.M. Marago, ACS Nano 5 (2011) 905–913.
[13] R.C. Jin, G. Wu, Z. Li, C.A. Mirkin, G.C. Schatz, J. Am. Chem. Soc. 125 (2003) 1643.
[14] K. Kneipp, M. Moskovits, H. Kneipp, Surface-enhanced Raman Scattering: Physics and Applications, Springer, 2006.
[15] V. Amendola, M. Meneghetti, Adv. Funct. Mater. 22 (2012) 353–360.
[16] R. Esteban, A.G. Borisov, P. Nordlander, J. Aizpurua, Nat. Commun. 3 (2012) 825.
[17] V. Amendola, M. Meneghetti, S. Fiameni, S. Polizzi, G. Fracasso, A. Boscaini, M. Colombatti, Anal. Methods 3 (2011) 849–856.
[18] X. Qian, X.H. Peng, D.O. Ansari, Q. Yin-Goen, G.Z. Chen, D.M. Shin, L. Yang, A.N. Young, M.D. Wang, S. Nie, Nat. Biotechnol. 26 (2008) 83–90.
[19] N.L. Rosi, C.A. Mirkin, Chem. Rev. 105 (2005) 1547–1562.
[20] M. Meneghetti, A. Scarsi, L. Litti, G. Marcolongo, V. Amendola, M. Gobbo, M. Di Chio, A. Boscaini, G. Fracasso, M. Colombatti, Small 8 (2012) 3733–3738.
[21] V. Amendola, O.M. Bakr, F. Stellacci, Plasmonics 5 (2010) 85–97.
[22] M. Futamata, Y. Maruyama, M. Ishikawa, J. Phys. Chem. B 107 (2003) 7607–7617.
[23] S. Link, M.A. El-Sayed, Intern. Rev. Phys. Chem. 19 (2000) 409–453.
[24] A.O. Govorov, H.H. Richardson, Nano Today 2 (2007) 30–38.
[25] P.K. Pain, I.H. El-Sayed, M.A. El-Sayed, Nano Today 2 (2007) 18–29.
[26] J. Lakowicz, Y. Fu, Laser Photon. Rev. 3 (2009) 221–232.
[27] C.X. Zhang, Y. Zhang, X. Wang, Z.M. Tang, Z.H. Lu, Anal. Biochem. 320 (2003) 136–140.
[28] R.A. Farrer, F.L. Butterfield, V.W. Chen, J.T. Fourkas, Nano Lett. 5 (2005) 1139–1142.
[29] V. Amendola, D. Dini, S. Polizzi, J. Shen, K.M. Kadish, M.J. Calvete, M. Hanack, M. Meneghetti, J. Phys. Chem. C 113 (2009) 8688–8695.
[30] V. Amendola, G. Mattei, C. Cusan, M. Prato, M. Meneghetti, Synth. Met. 155 (2005) 283–286.
[31] H. Fang, C. Du, S. Qu, Y. Li, Y. Song, H. Li, H. Liu, D. Zhu, Chem. Phys. Lett. 364 (2002) 290–296.
[32] V. Amendola, M. Meneghetti, Self-Healing at the Nanoscale: Mechanisms and Key Concepts of Natural and Artificial Systems, CRC Press, 2012.
[33] V. Amendola, M. Meneghetti, J. Mater. Chem. 22 (2012) 24501–24508.

[34] V. Amendola, M. Meneghetti, Nanoscale 1 (2009) 74–88.
[35] O.D. Häberlen, S.C. Chung, M. Stener, N. Rösch, J. Chem. Phys. 106 (1997) 5189–5201.
[36] C. Burda, X. Chen, R. Narayanan, M.A. El-Sayed, Chem. Rev. 105 (2005) 1025–1102.
[37] B. Nikoobakht, M.A. El-Sayed, Chem. Mater. 15 (2003) 1957–1962.
[38] C. Noguez, J. Phys. Chem. C 111 (2007) 3806–3819.
[39] B. Palpant, B. Prével, J. Lermé, E. Cottancin, M. Pellarin, M. Treilleux, A. Perez, J.L. Vialle, M. Broyer, Phys. Rev. B 57 (1998) 1963–1970.
[40] E. Prodan, P. Nordlander, N.J. Halas, Chem. Phys. Lett. 368 (2003) 94–101.
[41] K. Nobusada, J. Phys. Chem. B 108 (2004) 11904–11908.
[42] T. Iwasa, K. Nobusada, J. Phys. Chem. C 111 (2007) 45–49.
[43] H. Häkkinen, M. Walter, H. Grönbeck, J. Phys. Chem. B 110 (2006) 9927–9931.
[44] P. Pyykkö, Angew. Chem. 43 (2004) 4412–4456.
[45] K.G. Dyall, K. Fægri Jr., Introduction to Relativistic Quantum Chemistry, Oxford University Press, New York, 2007.
[46] D.M. Wood, Phys. Rev. Lett. 46 (1981) 749.
[47] S. Malola, L. Lehtovaara, J. Enkovaara, H. Häkkinen, ACS Nano 7 (2013) 10263–10270.
[48] G. Piccini, R.W.A. Havenith, R. Broer, M. Stener, J. Phys. Chem. C 117 (2013) 17196–17204.
[49] S. Bernadotte, F. Evers, C.R. Jacob, J. Phys. Chem. C 117 (2013) 1863–1878.
[50] N. Durante, A. Fortunelli, M. Broyer, M. Stener, J. Phys. Chem. C 115 (2011) 6277–6282.
[51] H-Ch Weissker, C. Mottet, Phys. Rev. B 84 (2011) 165443.
[52] S. Chen, R.S. Ingram, M.J. Hostetler, J.J. Pietron, R.W. Murray, T.G. Schaaff, J.T. Khoury, M.M. Alvarez, R.L. Whetten, Science 280 (1998) 2098–2101.
[53] S. Chen, R.W. Murray, J. Phys. Chem. B 103 (1999) 9996–10000.
[54] R.P. Andres, T. Bein, M. Dorogi, S. Feng, J.I. Henderson, C.P. Kubiak, W. Mahoney, R.G. Osifchin, R. Reifenberger, Science 272 (1996) 1323–1325.
[55] S. Chen, J. Am. Chem. Soc. 122 (2000) 7420–7421.
[56] S. Chen, R. Pei, J. Am. Chem. Soc. 123 (2001) 10607–10615.
[57] A. Arieh, R.M. Ratner, Chem. Phys. Lett. 29 (1974) 277–283.
[58] S. Chen, Z. Zhao, H. Liu, Annu. Rev. Phys. Chem. 64 (2013) 221–245.
[59] M. Brust, D. Bethell, C.J. Kiely, D.J. Schiffrin, Langmuir 14 (1998) 5425.
[60] L.-P. Xu, S. Chen, Chem. Phys. Lett. 468 (2009) 222–226.
[61] P.J. Thomas, G.U. Kulkarni, C.N.R. Rao, Chem. Phys. Lett. 321 (2000) 163–168.
[62] F.-R.F. Fan, A.J. Bard, Science 277 (1997) 1791–1793.
[63] L.Y. Gorelik, A. Isacsson, M.V. Voinova, B. Kasemo, R.I. Shekhter, M. Jonson, Phys. Rev. Lett. 80 (1998) 4526.
[64] J. Park, A.N. Pasupathy, J.I. Goldsmith, C. Chang, Y. Yaish, J.R. Petta, M. Rinkoski, J.P. Sethna, H.D. Abruña, P.L. McEuen, D.C. Ralph, Nature 417 (2001) 722–725.
[65] W.M. Lackowski, J.K. Campbell, G. Edwards, V. Chechik, R.M. Crooks, Langmuir 15 (1999) 7632–7638.
[66] Y. Guo, L.M. Chen, Y. Song, P.G. Hu, S.W. Chen, Sci. Adv. Mater. 6 (2014) 1060–1067 (accepted).
[67] K.C. Chan, P.F. Lee, J.Y. Dai, Appl. Phys. Lett. 92 (2008) 143117.
[68] E.A. Speets, B. Dordi, B.J. Ravoo, N. Oncel, A.-S. Hallbäck, H.J.W. Zandvliet, B. Poelsema, G. Rijnders, D.H.A. Blank, D.N. Reinhoudt, Small 1 (2005) 395–398.
[69] F.P. Zamborini, M.C. Leopold, J.F. Hicks, P.J. Kulesza, M.A. Malik, R.W. Murray, J. Am, Chem. Soc. 124 (2001) 8958–8964.
[70] J.F. Hicks, A.C. Templeton, S. Chen, K.M. Sheran, R. Jasti, R.W. Murray, J. Debord, T.G. Schaaff, R.L. Whetten, Anal. Chem. 71 (1999) 3703–3711.

[71] Y. Yang, S. Chen, Nano Lett. 3 (2003) 75–79.
[72] F. Remacle, R.D. Levine, J. Am. Chem. Soc. 122 (2000) 4084–4091.
[73] S. Pradhan, J. Sun, F. Deng, S. Chen, Adv. Mater. 18 (2006) 3279–3283.
[74] B. Sampedro, P. Crespo, A. Hernando, R. Litrán, J.C. Sánchez López, C. López Cartes, A. Fernández, J. Ramírez, J. González Calbet, M. Vallet, Phys. Rev. Lett. 91 (2003) 237203.
[75] M.A. Garcia, M.L. Ruiz-González, G.F. de la Fuente, P. Crespo, J.M. González, J. Llopis, J.M. González-Calbet, M. Vallet-Regí, A. Hernando, Chem. Mater. 19 (2007) 889–893.
[76] P. Crespo, R. Litran, T.C. Rojas, M. Multigner, J.M. de la Fuente, J.C. Sanchez-Lopez, M.A. Garcia, A. Hernando, S. Penades, A. Fernandez, Phys. Rev. Lett. 93 (2004) 087204.
[77] J.S. Garitaonandia, M. Insausti, E. Goikolea, M. Suzuki, J.D. Cashion, N. Kawamura, H. Ohsawa, I. Gil de Muro, K. Suzuki, F. Plazaola, T. Rojo, Nano Lett. 8 (2008) 661–667.
[78] H. Hori, T. Teranishi, Y. Nakae, Y. Seino, M. Miyake, S. Yamada, Phys. Lett. A 263 (1999) 406–410.
[79] M. Brust, M. Walker, D. Bethell, D.J. Schiffrin, R. Whyman, J. Chem. Soc. Chem. Commun. 801 (1994).
[80] P. Crespo, M.A. Garcia, E. Fernández Pinel, M. Multigner, D. Alcántara, J.M. de la Fuente, S. Penadés, A. Hernando, Phys. Rev. Lett. 97 (2006) 177203.
[81] [a] P. Zhang, T.K. Sham, Appl. Phys. Lett. 81 (2002) 736.
[b] P. Zhang, P.S. Kim, T.K. Sham, Appl. Phys. Lett. 82 (2003) 1470.
[82] M.A. Garcia, J. de la Venta, P. Crespo, J. Llopis, S. Penadés, A. Fernández, A. Hernando, Phys. Rev. B. 72 (2005) 241403.
[83] I. Carmeli, G. Leitus, R. Naaman, S. Reich, Z. Vager, J. Chem. Phys. 118 (2003) 10372.
[84] E. Guerrero, M.A. Muñoz-Marquez, E. Fernandez-Pinel, P. Crespo, A.Hernando, A. Fernandez, J. Nanopart. Res. 10 (2008) 179.
[85] E. Guerrero, T.C. Rojas, M. Multigner, P. Crespo, M.A. Muñoz-Márquez, M.A. García, A. Hernando, A. Fernández, Acta Mater. 55 (2007) 723.
[86] J.M. de la Fuente, D. Alcantara, P. Eaton, P. Crespo, T.C. Rojas, A. Fernandez, A. Hernando, S. Penades, J. Phys. Chem. B 110 (2006) 13021.
[87] Y. Yamamoto, T. Miura, M. Suzuki, N. Kawamura, H. Miyagawa, T. Nakamura, K. Kobayashi, T. Teranishi, H. Hori, Phys. Rev. Lett. 93 (2004) 116801.
[88] J. de la Venta, V. Bouzas, A. Pucci, M.A. Laguna-Marco, D. Haskel, S.G.E. te Velthuis, A. Hoffmann, J. Lal, M. Bleuel, G. Ruggeri, C. de Julián Fernández, M.A. García, J. Nanosci. Nanotechnol. 9 (2009) 6434–6438.
[89] H. Hori, Y. Yamamoto, T. Iwamoto, T. Miura, T. Teranishi, M. Miyake, Phys. Rev. B 69 (2004) 174411.
[90] P. de la Presa, M. Multigner, J. de la Venta, M.A. Garcia, M.L. Ruiz-Gonzalez, J. Appl. Phys. 100 (2006) 123915.
[91] [a] M.A. Muñoz-Márquez, E. Guerrero, A. Fernández, P. Crespo, A. Hernando, R. Lucena, J.C. Conesa, J. Nanopart Res. 12 (2010) 1307–1318.
[b] E. Guerrero, M.A. Muñoz-Márquez, A. Fernández, P. Crespo, A. Hernando, R. Lucena, J.C. Conesa, J. Appl. Phys. 107 (2010) 064303.
[92] M. Suda, N. Kameyama, M. Suzuki, N. Kawamura, Y. Einaga, Angew. Chem. Int. Ed. 47 (2008) 160–163.
[93] A. Ayuela, P. Crespo, M.A. Garcia, A. Hernando, P.M. Echenique, New J. Phys. 14 (2012).
[94] Z. Vager, R. Naaman, Phys. Rev. Lett. 92 (2004) 087205.
[95] A. Hernando, P. Crespo, M.A. García, Phys. Rev. Lett. 96 (2006) 057206.
[96] A. Hernando, P. Crespo, M.A. García, E.F. Pinel, J. de la Venta, A. Fernández, S. Penadés, Phys. Rev. B 74 (2006) 052403.

[97] A. Hernando, M.A. García, Phys. Rev. Lett. 96 (2006) 029703.
[98] O. López-Acevedo, H. Tsunoyama, T. Tsukuda, H. Häkkinen, C.M. Aikens, J. Am. Chem. Soc. 132 (2010) 8210–8218.
[99] P.D. Jadzinsky, G. Calero, C.J. Ackerson, D.A. Bushnell, R.D. Kornberg, Science 318 (2007) 430–733.
[100] M.W. Heaven, A. Dass, P.S. White, K.M. Holt, R.W. Murray, J. Am. Chem. Soc. 130 (2008) 3754–3755.
[101] J.A. Alonso, Chem. Rev. 100 (2000) 637–678.
[102] Y. Yourdshahyan, A.M. Rappe, J. Chem. Phys. 117 (2002) 825.
[103] C. González, Y. Simón-Manso, M. Marquez, V. Mujica, J. Phys. Chem. B 110 (2006) 687–691.
[104] W. Luo, S.J. Pennycook, S.T. Pantelides, Nano Lett. 7 (2007) 3134–3137.
[105] L. Puerta, H.J. Franco, J. Murgich, C. Gonzalez, Y. Simon-Manso, V. Mujica, J. Phys. Chem. A 112 (2008) 9771–9783.
[106] A. Hernando, P. Crespo, M.A. García, M. Coey, A. Ayuela, P.M. Echenique, Phys. Status Solidi B 248 (2011) 2352.
[107] G. te Velde, F.M. Bickelhaupt, E.J. Baerends, C.F. Guerra, S.J.A. van Gisbergen, J.G. Snijders, T. Ziegler, J. Comput. Chem. 22 (2001) 931–967.
[108] E. van Lenthe, A.E. Ehlers, E.J. Baerends, J. Chem. Phys. 110 (1999) 8943.
[109] J.P. Perdew, K. Burke, M. Ernzerhof, Phys. Rev. Lett. 77 (1991) 3865.
[110] B.D. Yu, M. Scheffler, Phys. Rev. B 56 (1997) 15569(R).
[111] A. Ayuela, M.J. Puska, R.M. Nieminen, J.A. Alonso, Phys. Rev. B 72 (2005) 161403(R).
[112] P. Gambardella, S. Rusponi, M. Veronese, S.S. Dhesi, C. Grazioli, A. Dallmeyer, I. Cabria, R. Zeller, P.H. Dederichs, K. Kern, C. Carbone, H. Brune, Science 300 (2003) 1130.
[113] T. Chakraborty, P. Pietiläinen, Phys. Rev. B 50 (1994) 8460–8468.
[114] A. Fuhrer, S. Lüscher, T. Ihn, T. Heinzel, K. Ensslin, W. Wegscheider, M. Bichler, Nature 413 (2001) 822–825.
[115] K. Rumpf, P. Granitzer, H. Krenn, J. Phys. Condens. Matter 20 (2008) 454221.
[116] J. Tempere, I.F. Silvera, J.T. Devreese, Phys. Rev. B 65 (2002) 195418.
[117] D. Huang, G. Gumbs, Phys. Lett. A 167 (1992) 396–400.
[118] N. Sánchez, S. Gallego, M.C. Muñoz, Phys. Rev. Lett. 101 (2008) 067206.
[119] S. LaShell, B.A. McDougall, E. Jensen, Phys. Rev. Lett. 77 (16) (1996) 3419–3422.
[120] A. Hernando, M.A. García, J. Nanopart. Res. (2011). http://dx.doi.org/10.1007/s11051-011-0257-7.
[121] A. Hernando, E. Herrero, M. Vázquez, J. Alonso, A. González, G. Rivero, J.M. Rojo, M. Vallet-Regi, J. González Calbet, Phys. Rev. B 56 (1997) 7800–7803.
[122] J.C. Azćarate, G. Corthey, E. Pensa, C. Vericat, M.H. Fonticelli, R.C. Salvarezza, P. Carro, J. Phys. Chem. Lett. 4 (2013) 3127–3138 (and references therein).
[123] B. Hvolbæk, T.V.W. Janssens, B.S. Clausen, H. Falsig, C.H. Christensen, J.K. Nørskov, Nano Today 2 (2007) 14–18.
[124] Z.W. Wang, R.E. Palmer, Nano Lett. 12 (2012) 91–95.
[125] H. Häkkinen, Nat. Chem. 4 (2012) 443–445 (and references therein).
[126] H. Häkkinen, Chem. Soc. Rev. 37 (2008) 184–1859 (and references therein).
[127] C. Zeng, H. Qian, T. Li, G. Li, N.L. Rosi, B. Yoon, R.N. Barnett, R.L. Whetten, U. Landman, R. Jin, Angew. Chem. Int. Ed. 51 (2012) 13114–13118.
[128] H. Yang, Y. Wang, H. Huang, L. Gell, L. Lehtovaara, S. Malola, H. Häkkinen, N. Zheng, Nat. Commun. 4 (2013) 2422.
[129] C.L. Heinecke, T.W. Ni, S. Malola, V. Mäkinen, O.A. Wong, H. Häkkinen, C.J. Ackerson, J. Am. Chem. Soc. 134 (2012) 13316–13322.

[130] G.A. DeVries, M. Brunnbauer, Y. Hu, A.M. Jackson, B. Long, B.T. Neltner, O. Uzun, B.H. Wunsch, F. Stellacci, Science 315 (2007) 358–361.
[131] L. Beqa, D. Deschamps, S. Perrio, A.C. Gaumont, S. Knoppe, T. Bürgi, J. Phys. Chem. C 117 (2013) 21619–21625.
[132] H. Qian, W.T. Eckenhoff, Y. Zhu, T. Pintauer, R. Jin, J. Am. Chem. Soc. 132 (2010) 8280–8281.
[133] I. Dolamic, S. Knoppe, A. Dass, T. Bürgi, Nat. Commun. 3 (2012) 798.
[134] S. Knoppe, R. Azoulay, A. Dass, T. Bürgi, J. Am. Chem. Soc. 134 (2012) 20302–20305.
[135] M. Zhu, H. Qian, X. Meng, S. Jin, Z. Wu, R. Jin, Nano Lett. 11 (2011) 3963–3969.
[136] S. Knoppe, N. Kothalawala, V.R. Jupally, A. Dass, T. Bürgi, Chem. Commun. 48 (2012) 4630–4632.
[137] Z. Ma, S. Dai, ACS Catal. 1 (2011) 805–816.
[138] R. Nafria, P. Ramírez de la Piscina, N. Homs, J.R. Morante, A. Cabot, U. Diaze, A. Corma, J. Mater. Chem. A 1 (2013) 14170–14176.
[139] M. Cargnello, C. Gentilini, T. Montini, E. Fonda, S. Mehraeen, M. Chi, M. Herrera-Collado, N.D. Browning, S. Polizzi, L. Pasquato, P. Fornasiero, Chem. Mater. 22 (2010) 4335–4345.
[140] M. Chen, D.W. Goodman, Chem. Soc. Rev. 37 (2008) 1860–1870.
[141] M.S. Chen, D.W. Goodman, Science 306 (2004) 252–255.
[142] H. Yoshida, Y. Kuwauchi, J.R. Jinschek, K. Sun, S. Tanaka, M. Kohyama, S. Shimada, M. Haruta, S. Takeda, Science 335 (2012) 317–319.
[143] M. Haruta, Angew. Chem. Int. Ed. 53 (2014) 52–56.
[144] J. Guzman, S. Carrettin, A. Corma, J. Am. Chem. Soc. 127 (2005) 3286–3287.
[145] N. Ta, J. Liu, S. Chenna, P.A. Crozier, Y. Li, A. Chen, W. Shen, J. Am. Chem. Soc. 134 (2012) 20585–20588.
[146] M. Farnesi Camellone, S. Fabris, J. Am. Chem. Soc. 131 (2009) 10473–10483.
[147] Y. Kuwauchi, H. Yoshida, T. Akita, M. Haruta, S. Takeda, Angew. Chem. Int. Ed. 51 (2012) 7729–7733.
[148] M.S. Ide, R.J. Davis, Acc. Chem. Res. 47 (2014) 825–833.
[149] T. Yan, J. Gong, D.W. Flaherty, C.B. Mullins, J. Phys. Chem. C 115 (2011) 2057–2065.
[150] M. Ojeda, B.-Z. Zhan, E. Iglesia, J. Catal. 285 (2012) 92–102.
[151] X. Nie, H. Qian, Q. Ge, H. Xu, R. Jin, ACS Nano 6 (2012) 6014–6022.
[152] Y. Zhu, H. Qian, R. Jin, Chem. Eur. J. 16 (2010) 11455–11462.
[153] Y. Liu, H. Tsunoyama, T. Akita, S. Xie, T. Tsukuda, ACS Catal. 1 (2011) 2–6.
[154] R. Juarez, S.F. Parker, P. Concepcion, A. Corma, H. Garcia, Chem. Sci. 1 (2010) 731–738.
[155] A. Lyalin, T. Taketsugu, Farad. Discuss. 152 (2011) 185–201.
[156] A. Corma, H. Garcia, Chem. Soc. Rev. 37 (2008) 2096–2126.
[157] M. Stratakis, H. Garcia, Chem. Rev. 112 (2012) 4469–4506.
[158] Y. Mikami, A. Dhakshinamoorthy, M. Alvaro, H. Garcia, Catal. Sci. Tech. 3 (2013) 58–69.
[159] Y. Zhu, H. Qian, B.A. Drake, R. Jin Angew, Chem. Int. Ed. 49 (2010) 1295–1298.
[160] A. Shivhare, S.J. Ambrose, H. Zhang, R.W. Purves, R.W.J. Scott, Chem. Commun. 49 (2013) 276–278.
[161] Y. Zhu, H. Qian, M. Zhu, R. Jin, Adv. Mater. 22 (2010) 1915–1920.
[162] Y. Zhu, Z. Wu, C. Gayathri, H. Qian, R.R. Gil, R. Jin, J. Catal. 271 (2010) 155–160.
[163] R.P. Carney, G.A. DeVries, C. Dubois, H. Kim, J.Y. Kim, C. Singh, P.K. Ghorai, J.B. Tracy, R.L. Stiles, R.W. Murray, S.C. Glotzer, F. Stellacci, J. Am. Chem. Soc. 130 (2008) 798–799.
[164] Q.K. Ong, J. Reguera, P. Jacob Silva, M. Moglianetti, K. Harkness, M. Longobardi, K.S. Mali, C. Renner, S. De Feyter, F. Stellacci, ACS Nano 7 (2013) 8529–8539.

[165] Q.K. Ong, J. Reguera, P. Jacob Silva, M. Moglianetti, K. Harkness, M. Longobardi, K.S. Mali, C. Renner, S. De Feyter, F. Stellacci, Langmuir 29 (2013) 13723−13734.
[166] K.M. Harkness, A. Balinski, J.A. McLean, D.E. Cliffel, Angew. Chem. Int. Ed. 50 (2011) 10554−10559.
[167] X. Liu, M. Yu, H. Kim, M. Mameli, F. Stellacci, Nat. Commun. 3 (2012) 1182.
[168] C. Singh, P.K. Ghorai, M.A. Horsch, A.M. Jackson, R.G. Larson, F. Stellacci, S.C. Glotzer, Phys. Rev. Lett. 99 (2007) 226106.
[169] I.C. Pons-Siepermann, S.C. Glotzer, ACS Nano 6 (2012) 3919−3924 (and reference therein).
[170] F. Romano, E. Sanz, F. Sciortino, J. Chem. Phys. 134 (2011) 174502.
[171] A. Centrone, E. Penzo, M. Sharma, J.W. Myerson, A.M. Jackson, N. Marzari, F. Stellacci, Proc. Natl. Acad. Sci. U.S.A. 105 (2008) 9886−9891.
[172] A. Verma, O. Uzun, Y. Hu, Y. Hu, H.-S. Han, N. Watson, S. Chen, D.J. Irvine, F. Stellacci, Nat. Mater. 7 (2008) 588−595.
[173] R.C. Van Lehn, P.U. Atukorale, R.P. Carney, Y.−S. Yang, F. Stellacci, D.J. Irvine, A. Alexander-Katz, Nano Lett. 13 (2013) 4060−4067.
[174] A. Ghosh, S. Basak, B.H. Wunsch, R. Kumar, F. Stellacci, Angew. Chem. Int. Ed. 50 (2011) 7900−7905.
[175] E.S. Cho, J. Kim, B. Tejerina, T.M. Hermans, H. Jiang, H. Nakanishi, M. Yu, A.Z. Patashinski, S.C. Glotzer, F. Stellacci, B.A. Grzybowski, Nat. Mater. 11 (2012) 978−985.
[176] P. Posocco, C. Gentilini, S. Bidoggia, A. Pace, P. Franchi, M. Lucarini, M. Fermeglia, S. Pricl, L. Pasquato, ACS Nano 6 (2012) 7243−7253.
[177] D. Zaramella, P. Scrimin, L.J. Prins, J. Am. Chem. Soc. 134 (2012) 8396−8399.
[178] G. Pieters, A. Cazzolaro, R. Bonomi, L.J. Prins, Chem. Commun. 48 (2012) 1916−1918.
[179] C. Gentilini, F. Evangelista, P. Rudolf, P. Franchi, M. Lucarini, L. Pasquato, J. Am. Chem. Soc. 130 (2008) 15678−15682.
[180] B. Perrone, S. Springhetti, F. Ramadori, F. Rastrelli, F. Mancin, J. Am. Chem. Soc. 135 (2013) 11768−11771.
[181] C.K. Kim, P. Ghosh, C. Pagliuca, Z.-J. Zhu, S. Menichetti, V.M. Rotello, J. Am. Chem. Soc. 131 (2009) 1360−1361.